Probing the Optoelectronic Behavior of 2D Nanomaterials Synthesized by Laser Ablation and Hydrothermal Method

March 2024

SHINDE VINAYAK BHAUSAHEB

Tokushima University
Graduate School of Advanced Technology and Science
Systems Innovation Engineering, Optical Systems Engineering
Doctoral Course

Abstract

The synthesis of well-faceted tungsten suboxide (WO_{3-x}) produced by laser ablation in a liquid medium. The tungsten disulfide (WS_2) was used as bulk material, while the mixer of water and ethanol was used as a solvent. The laser ablation was carried out using ns second Nd:YAG laser (Second harmonic, 532 nm) with an output power of 600 mW and an ablation time of 20 minutes. The structural properties and morphological features of WO_{3-x} were analyzed by UV–Vis spectroscopy, FE-SEM, EDS, and XRD. The UV-vis spectra and EDS spectra revealed the formation of sub-oxide tungsten oxide. While XRD spectra show that the bulk WS_2 was turned into sub-oxide tungsten oxide (WO_{3-x}). The SEM images demonstrated a self-assembled petal-like flake structure made up of ultra-thin nanosheets with a thickness of less than 20 nm. A well-defined WO_{3-x} petal-like nanosheet is proposed to be useful for prospective applications in optoelectronic devices. Also, tungsten suboxide/tin oxide (WO_{3-x}/SnO_2) composites were successfully prepared via laser ablation method. The prepared WO_{3-x}/SnO_2 binary composite was employed as a photocatalyst for the photodecomposition of methylene blue (MB). The photocatalytic performance of the binary composites was superior to that of WO_{3-x} and SnO_2 when exposed to LED light. The obtained materials were characterized by several microscopic and spectroscopic techniques, namely EDS, FE-SEM, and UV-vis spectroscopy. According to UV-vis spectroscopy, the formation of tungsten suboxide, crystalline SnO_2 nanoparticles, and visible region absorption of composite indicates that the composite is suitable for photocatalytic activity. The petal-like structure of WO_{3-x} was covered with SnO_2 octahedron crystals, as demonstrated by the SEM images of the WO_{3-x}/SnO_2. Moreover, elemental mapping was carried out using EDS to ensure the existence of SnO_2, WO_{3-x}, and the binary composite of WO_{3-x} and SnO_2. The matching of XRD peak positions with JCPDS standards provides evidence that the binary composite was created. The improved photocatalytic activity of the WO_{3-x}/ SnO_2 composite can be directly accredited to the presence of SnO_2, which may

lead to an increase in the separation efficiency of electron-hole pairs. The 84.4 % of MB removal was achieved after 60 minutes of illumination compared to 41.58 % synthesized SnO_2 and 25.38 % of WO_{3-x}. It was one of the most photoactive WO_{3-x} based photocatalysts for methylene blue (MB) photodecomposition. Also, WS_2/GO/Au ternary composite was synthesized using nanosecond laser ablation followed by adding Au using the hydrothermal method. UV-Vis, Raman, XRD, and FE-SEM were used to examine the microstructure, morphology, and spectroscopic properties of the samples that had been produced. The UV-vis spectra suggest the formation of a ternary composite, and FE-SEM shows morphology as Au nanoparticles with a size ranging from 20-30 nm are perfectly mixed with WS_2 nanosheets, which can be seen on GO sheets. EDS-SEM images indicate the availability of all elements in prepared samples and the formation of a ternary composite of WS_2/GO/Au. XRD and Raman spectroscopy confirm the crystalline nature of AuNPs and WS_2 and suggest the transformation of GO into rGO. The prepared pristine (WS_2), binary (WS_2/GO), and ternary composite show the capability for methylene blue degradation under UV-light irradiation as 41.85 %, 48.27 %, and 83.17 %, respectively. The improved photocatalytic activity of the multicomponent has been demonstrated by nanostructure catalysts with specific morphology due to their exceptional electron transport characteristics.

Acknowledgment

I am, profoundly thankful to Dr. Pankaj Koinkar for his expert guidance and unwavering enthusiasm in my three-year Ph.D. journey. His mentorship kept me engaged, imparted valuable optical science and physics lessons, and significantly impacted my academic growth. His kindness, generosity, and ongoing support are invaluable, and his guidance has advanced both my research and life. Heartfelt thanks to Dr. Pankaj Koinkar.

I extend a special appreciation to Professor Akihiro Furube for his invaluable assistance, guidance, and timely help throughout my Ph.D. His insightful discussions, research advice, and unwavering encouragement have been a constant source of motivation and support. I am also grateful to Dr. Tetsuro Katayama for his dedicated support and guidance, offering valuable insights and advice numerous times during my Ph.D. journey. I am also thankful to Prof. Toshihiro Moriga for his invaluable support, guidance, and help in characterizing the samples. I extend a big thanks to Dr. Masatsugu Oishi for his help in conducting the XRD characterization. I want to express my gratitude to our collaborator, Professor R. B. Sathe, for his significant contributions to our research efforts. I would like to acknowledge the indispensable assistance provided by technical staff Mr. Satoshi Sugano who played a crucial role in supporting my experiments.

My heartfelt thanks go to the Heiwa-Nakajima Foundation, Japan, for their unwavering support through the Heiwa-Nakajima Scholarships program, providing financial and moral support throughout my Ph.D. I also really appreciate Mrs. Aparna Koinkar for her support from the start of the introduction to Tokushima University and her kindness, help, and Indian dinners offered, which gave homely feeling out of the home.

I am thankful to my Indian friends and colleagues at the C3 lab, with special mention to Mr. Maeda, who was always there by my side to make “Tokushima life better” with his unwavering support and camaraderie.

Above all, I owe a debt of gratitude to my parents, Parigha and Bhausaheb Shinde, whose support and values have grown even more significant with time. I am also profoundly thankful for the remarkable lady who is the mother of my two children, Mrs. Dipali. Her unwavering and unconditional support has been the bedrock upon which I have built my academic and personal endeavors. Without her steadfast encouragement, understanding, and partnership, I would not have had the courage or the ability to take this significant step in my academic and professional life. Her contributions to my journey are immeasurable, and I am deeply grateful for her presence in my life.

Dedicated to my son Shantanu and daughter Vidhi

List of Figures

Chapter 1

Chapter 2

Chapter 3

Chapter 4

Chapter 5

Abbreviations

2D	Two dimensional
UV-vis	Ultraviolet-visible
FE-SEM	Field emission-scanning electron microscopy
TEM	Transmission electron microscopy
XRD	X-ray diffraction
ns	Nanosecond
WS_2	Tungsten disulfide
AuNP	Gold nanoparticle
SnO_2	Tin oxide
Nd:YAG	Neodymium-doped yttrium aluminium garnet
MB	Methylene blue
GO	Graphene oxide
TMD	Transition metal dichalcogenides
PLAL	Pulse laser ablation in liquid
rGO	Reduced graphene oxide
EDS	Energy-dispersive x-ray spectroscopy

Chapter 1: Introduction

1.1 A brief introduction of two-dimensional (2D) materials

In recent years, scientists have achieved advancements with materials based on graphene, which is super thin and made of carbon. This progress led to the discovery of other thin materials useful for different research purposes. These materials are called 2D nanomaterials, and they include things like transition metal dichalcogenides, topological insulators (TIs), phosphorene, black phosphorus, hexagonal boron nitride (h-BN), Antimonene, Bismuthene, metal-organic framework, and MXenes (2D metal carbides and nitrides), etc. Researchers are

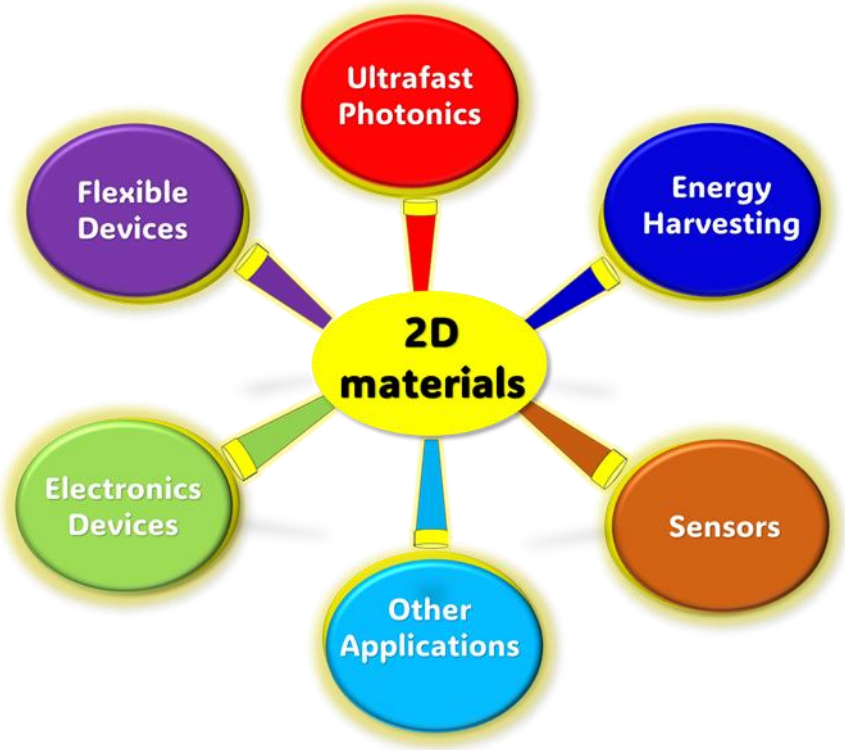

Fig. 1: Schematic illustration of different kinds of typical 2D nanomaterials and its applications.

excited about 2D nanomaterials because they have properties that make them good for medical devices, imaging, drug delivery, and tissue engineering [1-4]. Research on these materials has been growing, especially for things like MOFs, TMDs, Tis, and MXenes, which seem to have great potential for medical use. These 2D nanomaterials have two amazing features that set

them apart from other nanomaterials. First, as a researcher, we can control how they react to light by changing the number of layers or mixing them with other nanoparticles of noble metals. Second, we can change their behavior by adding different molecules to their surface, and this makes them suitable for electrochemical applications. Because of this, 2D TMDs can be used in applications like ultrafast photonics, energy harvesting, sensors, flexible devices, electronic devices, etc., due to their good optical, chemical, and electrical properties as shown in Fig. 1 [5].

1.2 Tungsten disulfide (WS_2) and molybdenum disulfide (MoS_2)

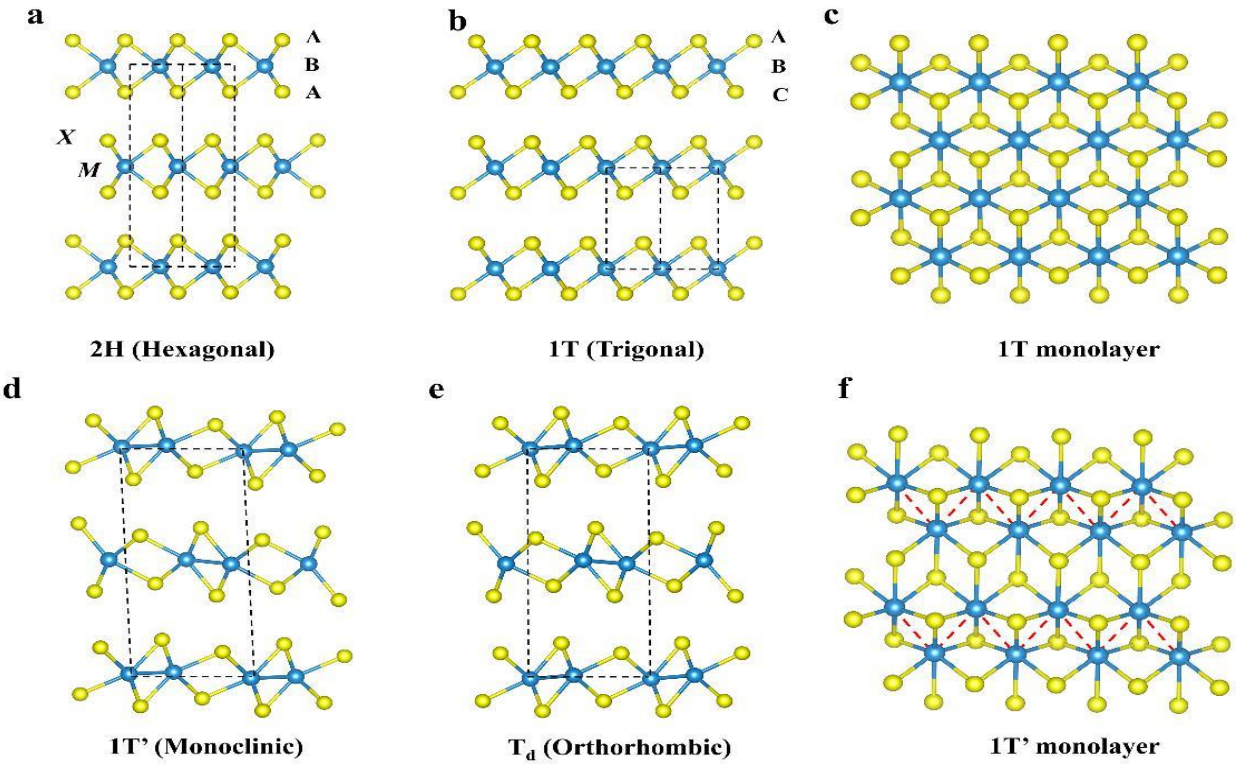

Fig. 2: Tungsten disulfide and Molybdenum disulfide phases, crystal structure, orientation

http://english.sim.cas.cn/Event/201906/t20190620_211901.html

The VIB layered transition metal disulfide (TMD) MX_2 (M= Mo, W; X= S, Se, Te) has considerable attention from researchers due to its rich crystal structure, strong spin-orbit coupling, unique electrical topologies, and physicochemical features. According to the coordination and stacking conditions of the layers, as shown in Fig. 2, the compounds can be

divided into three different phases: 1T phase formed by in-plane chemical coordination distortion Fig. 2 (d–f), 1T phase with an octahedral configuration, and 2H phase with a triangular prism configuration. The M-M sawtooth chain structure is formed in the plane by the metal atom M shifting along a certain direction in the plane Fig. 2 (f). There are numerous methods to stack the single layer 1T phase to produce [6-10]. Two-dimensional (2D) single-layer MoS_2 nanosheets have a direct bandgap of 1.8 eV, whereas the bulk MoS_2 material is said to have an indirect bandgap of 1.2 eV [11] and WS_2 exhibits a direct bandgap in its monolayer form (a single layer of atoms), Monolayer WS_2 has a direct bandgap of approximately 2.0 eV and the indirect bandgap of bulk or multilayer WS_2 typically falls within the range of 1.2 to 2.0 eV. The exact value can vary somewhat depending on factors such as the number of layers, strain, and the specific sample preparation methods used. However, a commonly cited value for the indirect bandgap of bulk WS_2 is around 1.4 eV. There are countless possibilities for general applications because the 2D MoS_2 absorption spectrum falls in the visible part of the electromagnetic spectrum [12-14].

1.3 Graphene oxide (GO)

Graphene offers advantages such as being environmentally friendly, biocompatible, and photostable compared to conventional 2D materials. Graphene is highly sought-after for various applications, including photocatalysis, solar cells, biosensing, and LED, because of its ~ 0 eV bandgap and good optical characteristics [15-18]. Graphite oxide sheets, now known as graphene oxide (GO), have a rich history dating back over 150 years, with B. C. Brodie's 1859 discovery and GO can be produced by chemical exfoliation of graphite. With oxygenated functional groups on its basal plane and edges, GO is initially insulating but quickly disperses in water. Through reduction, either by heat or chemical agents, some of the favorable properties of pristine graphitic sheets can be restored. Following the 2004 discovery of graphene, GO has regained interest as a precursor for graphene production. However, GO possesses intriguing

properties of its own, including flame retardancy, amphiphilicity, and the ability to form unique superstructures. It also finds applications in materials science, imaging, and nanofluidic systems [19-21]. Fig. 3 shows the schematic representation of GO synthesis by chemical oxidation using Hummer's method.

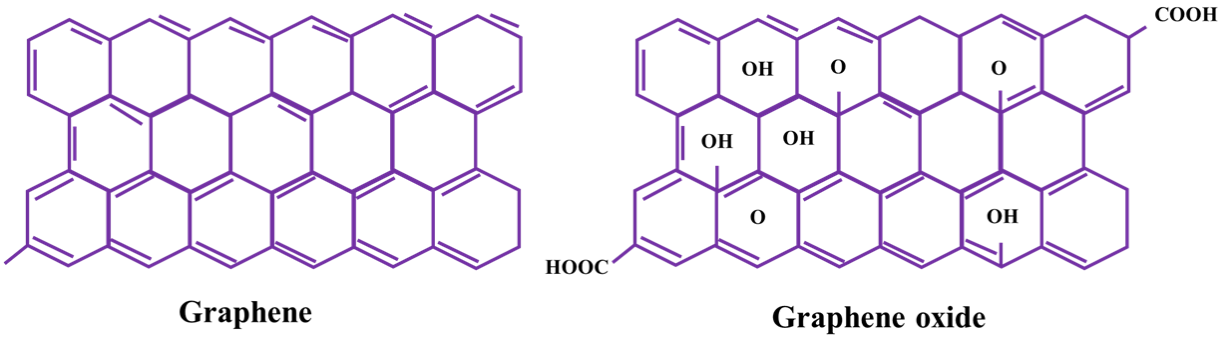

Fig. 3. Schematic illustration of GO synthesis by chemical oxidation using Hummer's method

1.4 Reduced graphene oxide (rGO)

Graphene oxide that has been chemically or thermally treated yields reduced graphene oxide (rGO). rGO is capable of restoring conductivity multiple times because of reduced oxygen and restored double-bonded aromatic carbon atoms [22]. In most cases, oxidized graphene oxide and graphite sheets are used to prepare rGO. L-ascorbic acid, sodium borohydride, hydrazine, and hydrazine hydrate are the most common reducing agents for converting GO to rGO. One can improve the properties of the composite to suit commercial uses by treating rGO with other chemicals or mixing rGO with other 2D materials to create new compounds [23].

1.5 Gold nanoparticles (AuNP)

Optical, chemical, and medical studies all frequently use gold as a material. Small gold nanoparticles (AuNPs) have exceptional optical properties that, when combined with their strong chemical stability and size-dependent electrochemical properties. These applications in electronics include conductive inks, nanoantennas, plasmonic devices, phase transfer phenomena, thermoelectric and nanoelectric devices, and memory devices [25-28]. These nanoparticles usually have a strong red color that changes from red to blue or purple as they

get bigger. To create AuNPs with unique features for specific applications, numerous chemical synthesis techniques, such as the Turkevich approach, the use of capping agents, the Brust-Schiffrin method, the Martin method, and sonolysis, are frequently used. AuNPs improve electrical conductivity and reinforce mechanical strength in nanocomposite materials. Additionally, they are adaptable for modifying the material properties due to their customizable size and form [29-33].

1.6 Synthesis methods of 2D materials

The synthesis of 2D materials involves various techniques tailored to their unique properties. Majorly distributed in 3 categories as 1) Mechanical exfoliation, known as the "Scotch tape method", 2) Chemical vapor deposition (CVD) grows 2D layers atom by atom on substrates, offering scalability for materials like MoS_2 and h-BN, and 3) Liquid-phase exfoliation (Laser ablation) employs solvents or surfactants to disperse layered materials into nanosheets, enabling the production of materials like black phosphorus. We are interested in the laser ablation technique for the synthesis of 2D nanomaterials [34].

1.7 Laser ablation technique

1.7.1 Principle

At the start of the laser ablation process, the high-energy photons from a laser are first absorbed, energizing the target material's electrons. The electronic energy of the material is raised by these photons as they move electrons into higher energy states or the conduction band. The energy is then quickly localized and heated, which may lead to phase shifts, vaporization, and the creation of a high-energy plasma. Depending on the ablation parameters, this extreme heating induces material removal that results in the formation of nanoparticles, nanowires, or thin films. Sometimes, absorbed energy causes plasma production, which is characterized by ionized materials ejecting charged particles and generating light. Target material characteristics

and ambient conditions, along with laser parameters including pulse duration, energy, wavelength, and repetition rate, all play a role in process control [35-36].

1.7.2 Nanosecond Nd:YAG laser

1.7.2.1. Properties

Nd:YAG lasers emit 1064 nm near-infrared light, which is valued for its ability to penetrate tissue and materials. These lasers have flexible operating modes, including continuous for laser pumping and pulsed for medical applications like ablation [37-38]. Longer pulse durations are suitable for welding and other heat-controlling applications. Nd:YAG lasers produce precise, low-divergence beams that are excellent for accurate engraving and cutting. They are solid-state, compact, and seamlessly fit into a variety of systems, necessitating effective cooling. Additionally, they permit frequency doubling, resulting in 532 nm green light for uses such as pointers and medical procedures. Due to their long-lasting dependability and endurance in industrial and scientific contexts, their many uses include materials processing, medical treatments, telecommunications, research, and defense. [39-40]

1.7.2.2. Applications

Nd:YAG lasers are widely used in nanophotonics, where cutting-edge research and technological advancement are made possible by the peculiar characteristics of these lasers. Plasmonic nanoparticles are created and worked on with Nd:YAG lasers to improve their optical qualities. These nanoparticles can focus and amplify light on the nanoscale, making them useful for applications in biosensors, imaging, and improved spectroscopy [41-42]. They are frequently constructed of noble metals like gold or silver. To create photonic crystal formations on the nanoscale, Nd:YAG lasers are essential. Due to the ability of these periodic nanostructures to influence light propagation, nanophotonic devices like optical filters, waveguides, and sensors have been created. At the nanoscale, integrated photonic circuits and

waveguides are accurately patterned using Nd:YAG lasers. These waveguides make it possible to manipulate and route light on a chip, which advances on-chip optical communication and signal processing equipment. The creation of metamaterials with subwavelength structures uses Nd:YAG lasers. Nanoplasmonic sensor devices with Nd:YAG laser integration enable ultrasensitive detection of chemical and biological substances at the nanoscale. These sensors are used in drug development, environmental monitoring, and medical diagnostics. For the application of quantum dots as nanoscale light emitters in quantum dot nanophotonics, Nd:YAG lasers are necessary. Advanced displays, quantum cryptography, and quantum computing are all impacted by this technology [43-47].

1.8 Hydrothermal method

1.8.1 Introduction

In order to establish a high-temperature, high-pressure environment, hydrothermal methods use an aqueous solution as a reaction system in a closed vessel. It has been created for almost 200 years and is extensively used in many disciplines, including materials science, earth science, metallurgy, physics, chemistry, and biology. To simulate the production of specific minerals and rocks found in nature, the procedure entails dissolving and recrystallizing compounds that are weakly soluble or insoluble under normal conditions. At relatively low temperatures, the hydrothermal process can be used to produce single crystals, create ceramic powders, carry out organic reactions, handle organic waste, and sinter ceramic materials. It has been continuously enhanced throughout time by incorporating methods like microwave heating, mechanical mixing, and electric fields to increase reaction kinetics and shorten experimental times [48, 50].

1.8.2 Properties and applications

Conventional hydrothermal synthesis techniques use conduction to heat the material. Improving the traditional hydrothermal approach has several benefits, such as rapid heating,

sensitive reactions, and even heating. These properties allow for the quick synthesis of nanoparticles with a homogeneous shape and restricted particle size distribution. The hydrothermal method may prepare samples that require a long time or are sensitive to temperature variations, making it particularly helpful for reactions with large temperature fluctuations and lengthy reaction times. Furthermore, the improved conventional hydrothermal procedures have been proven to be quicker, cleaner, and more cost-effective, leading to a useful method for the synthesis of new functional materials [48-49].

Applications for hydrothermal synthesis are numerous and spread across several industries. A variety of single crystals are grown by hydrothermal synthesis, which is vital for studying the characteristics and behavior of materials. Additionally, the hydrothermal process is utilized to create ceramic powders that are less agglomerated or ultra-finely agglomerated. These powders feature a restricted particle size range, fine crystals, controlled morphology, and excellent purity. It can be applied to finish specific organic processes, enabling the synthesis of organic molecules at high temperatures and pressures. Organic waste that endangers the environment can be treated using hydrothermal technology. These waste materials can decompose and be detoxified thanks to the high pressure and temperature conditions. Certain ceramic materials can be sintered using the hydrothermal method at relatively low temperatures, which reduces energy use and boosts the effectiveness of the sintering procedure. These uses demonstrate how versatile and significant hydrothermal synthesis is in materials science, earth science, metallurgy, physics, chemistry, and biology [48].

1.9 Photocatalysis

1.9.1. Introduction

Photocatalysis is a fascinating and highly relevant branch of chemistry that has gained significant attention and importance in recent years. It revolves around chemical reactions that

occur under the influence of light in the presence of a photocatalyst. This field of study has demonstrated immense potential for a wide range of applications, addressing some of the most pressing global challenges. One of the prominent applications of photocatalysis is in the realm of water purification. The process involves the use of photocatalysts to break down organic pollutants, and contaminants present in water sources when exposed to light. This technology has the potential to provide clean and safe drinking water, particularly in regions where water quality is a significant concern [51-54]. Photocatalysis plays a pivotal role in the generation of hydrogen as a clean and renewable energy source. With the ever-increasing global energy demand and concerns about climate change, hydrogen has emerged as a promising candidate to meet these challenges. Since 1972, research in the field of photocatalytic hydrogen production has been on the rise. Photocatalysis offers an economical and sustainable route for harnessing hydrogen by utilizing readily available resources such as water and sunlight. In addition to hydrogen, photocatalysis can also facilitate the production of oxygen. This has implications for both environmental and industrial applications. For instance, in closed environments like spacecraft or submarines, where a continuous supply of oxygen is crucial, photocatalytic oxygen production could provide a reliable solution [55-56]. Photocatalysis is utilized in the process of deionization, which involves the removal of ions from water. This is important in various industries, including electronics manufacturing and power generation, where the presence of ions may cause to equipment corrosion and reduced efficiency [57]. Photocatalysis has shown promise in the development of antibacterial materials and coatings. When exposed to light, certain photocatalysts can generate reactive oxygen species that have potent antibacterial properties. This has potential applications in healthcare, food packaging, and sanitation. The self-cleaning properties of certain materials, such as self-cleaning glass, are made possible through photocatalysis. These materials can break down organic contaminants on their surfaces when exposed to sunlight, reducing the need for manual cleaning and

maintenance [58]. The significance of photocatalysis extends beyond individual applications. It aligns with pressing demand for clean and sustainable energy sources, environmental protection, and the improvement of public health. As the world population grow and the standard of living rises, the demand for energy escalates exponentially. Harnessing the power of photocatalysis, which relies on abundant resources like water and sunlight, represents a promising avenue to meet this demand in an environmentally friendly manner. In conclusion, photocatalysis is a versatile and innovative field of chemistry with far-reaching implications for addressing global challenges. Its applications in water purification, hydrogen production, oxygen generation, deionization, antibacterial technology, and self-cleaning materials underscore its importance in creating a sustainable and cleaner future. The ongoing research and development in this field holds the key to unlocking its full potential for the benefit of humanity and the environment. [59]. The light-induced photo-oxidation of water utilizing metal oxide as a photocatalyst, such as MoS_2 and WS_2, is one of the potential ways to create hydrogen by photocatalysis [60-61].

1.9.2. Principle

Photocatalysts are semiconducting materials that use their large surface area and ability to move charges when exposed to light to accelerate the rate of reaction**.** When a photon participates in a chemical reaction, the system is known as photocatalytic. The catalysts facilitated the redox reaction by absorbing the reactant and photon photons, generating electrons and holes.

1.10 Purpose and significance of the research

1.10.1. Purpose:

The research that was carried out aims to advance the field of environmental remediation by investigating novel nanomaterials synthesized via nanosecond laser ablation and hydrothermal

methods to improve the photocatalytic degradation of methylene blue (MB) under visible light. Specifically, this study focuses on three distinct approaches.

1.10.1.1. Ternary composite of WS_2/GO/Au

The purpose is to explore the synergistic effects of tungsten disulfide (WS_2), graphene oxide (GO), and gold (Au) nanoparticles in primary, binary, and ternary composites. By utilizing laser ablation and hydrothermal methods, we seek to enhance MB degradation efficiency while capitalizing on the unique properties of each component.

1.10.1.2. Tungsten suboxide (WO_{3-x}) petal-like nanosheets

This segment investigates the synthesis of tungsten suboxide (WO_{3-x}) nanosheets using laser ablation. The objective is to create petal-like structures with improved visible light absorption capabilities, enabling more efficient MB degradation compared to conventional WO_3 materials.

1.10.1.3. WO_{3-x}/SnO_2 nanocomposites

This part of the research focuses on the synthesis of nanocomposites comprising tungsten suboxide (WO_{3-x}) and tin dioxide (SnO_2) using laser ablation. The primary aim is to enhance the photocatalytic performance of these materials under visible light, offering a promising solution for MB degradation and potentially other environmental applications.

1.10.2. Significance:

The significance of this research lies in its potential to revolutionize the field of photocatalysis for water purification and environmental remediation. By harnessing laser ablation synthesis techniques, we can tailor nanomaterials with unique properties, such as enhanced light absorption and catalytic activity. A well-defined WO_{3-x} petal-like nanosheet can be useful for applications in future optoelectronic devices. Also, 84.4 % of MB removal was achieved after 60 minutes of illumination with WO_{3-x}/SnO_2 as catalyst make it one of the photoactive WO_{3-x}

based photocatalysts for methylene blue (MB) photodecomposition and synthesized ternary composite WS_2/GO/Au shows almost ~83 % degradation of MB. These innovations hold promise for more efficient MB degradation, contributing to cleaner water sources and a sustainable environment. Furthermore, the insights gained from these studies could lead the way for the development of advanced photocatalytic materials with broader applications beyond MB degradation, addressing various environmental challenges on a global scale. Ultimately, this research aligns with the urgent need for cleaner and more efficient technologies to combat water pollution and promote environmental sustainability.

Chapter 2: Experimental

2.1 Synthesis of WO_{3-x} nanoflakes

This experiment used bulk WS_2 powder acquired from Sigma-Aldrich with an average sheet size of ~ 3-5 µm. A mixture of two different solvents, ethanol (10 mL) and distilled water (10 mL), was combined in a glass bottle. Following that, 10 mg of bulk WS_2 powder was added to the mixture. In separate glass bottles, four different samples were produced for the different laser ablation at times of 5, 10, 15, and 20 minutes. Prior to nanosecond (ns) laser ablation, these prepared samples in glass bottles underwent 10 minutes of sonication using a probe sonicator (VIOLAMO Sonicstar 85). All of the bottles were maintained under continuous magnetic stirring during ns laser ablation and were ablated with the second harmonic of a Nd:YAG laser (wavelength 532 nm, repetition frequency 10 Hz, pulse duration 10 ns, 800 mW) for varying periods (5 to 20 minutes). The bulk and laser ablated samples were then characterized using UV-vis spectroscopy (U-2010, Shimadzu), X-ray diffraction (Rigaku, Smart-Lab 9 kW), field emission scanning electron microscopy (FESEM, S4700, JEOL), and electron dispersive spectrometry (SEM-EDS, JSM-6510A, JEOL). The raman spectrum of bulk and laser ablated samples was analyzed using the raman microscopy with a Renishaw microscope set to 532 nm. Fig. 5 shows an experimental setup for obtaining nanoflakes.

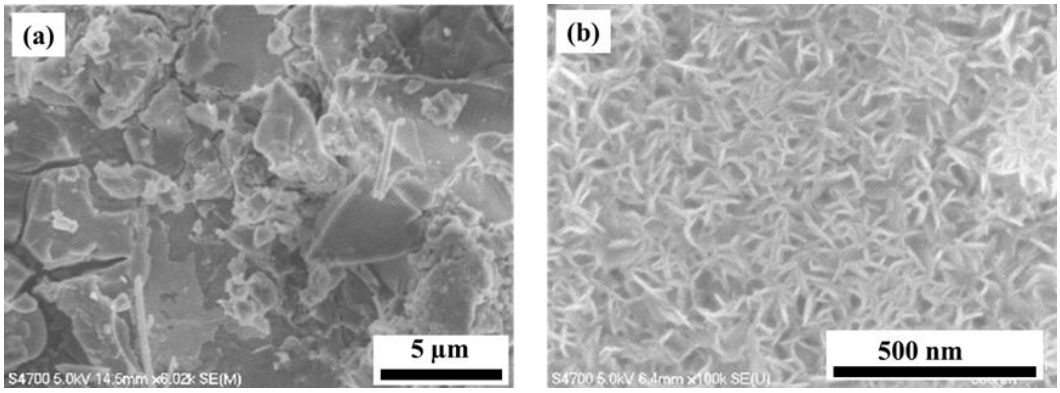

Fig. 4: SEM images of (a) bulk WS_2 and (b) WO_{3-x} nanoflakes (petal like)

The FESEM images of bulk WS_2 in fig. 4 (a) and the laser ablated WS_2 is shown in fig. 4 (b).

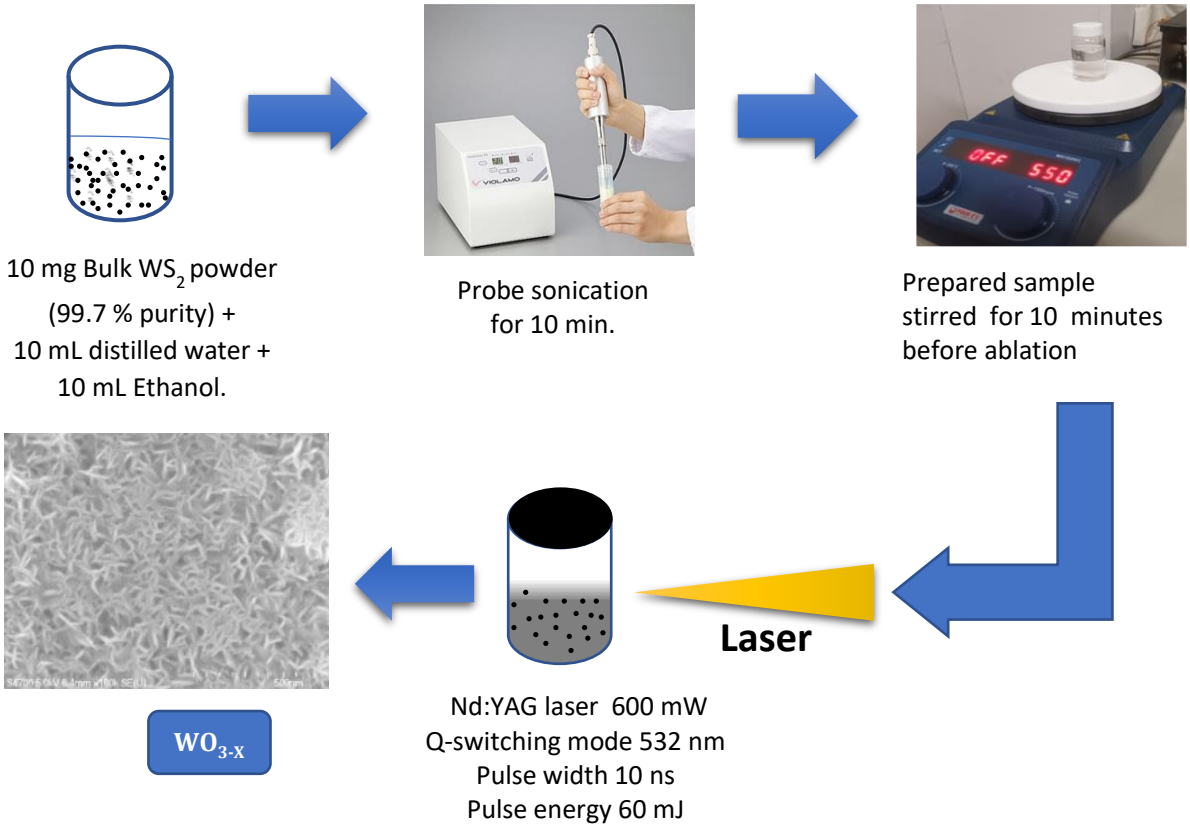

Fig. 5: Experimental setup for obtaining nanoflakes.

2.2 Synthesis of WO_{3-x}/SnO_2 nanocomposites

2.2.1 Preparation of WO_{3-x}

In this experiment, tungsten disulfide (WS_2) powder (10 mg) was used as a bulk material and added to an equal amount of distilled water (10 ml) and ethanol (10 ml) and then subjected to 10 minutes probe sonication using VIOLAMO Sonicstar 85 prior to nanosecond laser ablation. In this experiment, the bulk WS_2 powder with an average sheet size of about 4-6 µm was utilized. The sample was kept under constant magnetic stirring before ns laser ablation with the second harmonic of a Nd:YAG laser (532 nm, repetition frequency 10 Hz, 600 mW, 10 ns) for 20 minutes. The bulk and laser ablated samples were analyzed using UV-vis spectrophotometer (U-2010, Shimadzu), field emission scanning electron microscope (FESEM, S4700, JEOL), and electron dispersive spectrometer (SEM-EDS, JSM-6510A, JEOL).

2.2.2 Preparation of SnO_2

The bulk SnO powder bought from Sigma-Aldrich with an average sheet size of about a few µm was used. The SnO_2, having octahedron crystal-like structure, was fabricated using SnO (10 mg) as a bulk material by adding it to ethanol (20 ml), and the probe sonicated it for 10 minutes using VIOLAMO Sonicstar 85 before irradiating with Nd:YAG laser ablation. After that, the sample was exposed to ns laser ablation for 20 minutes with constant magnetic stirring. Nd:YAG laser of the second harmonic having a wavelength of 532 nm with the power of 600 mW was used for irradiation. The characterization of the prepared samples was carried out using UV-vis spectrophotometer (U-2010, Shimadzu), field emission scanning electron microscope (FESEM, S4700, JEOL), and electron dispersive spectrometer (SEM-EDS, JSM-6510A, JEOL), Raman (MicroRam-TE-US, Lambda Vision Inc., Sagamihara, Japan), XRD (Rigaku, Smart-Lab 9 kW).

2.2.3 Preparation of SnO_2/WO_{3-x}

A vapor evaporation technique was used to dry laser ablated WO_{3-x} and SnO_2 liquids. Resulting WO_{3-x} powder in blue color with octahedron phase and SnO_2 powder in white yellowish color was produced. The two powdered samples with 1 mg each were dissolved in 10 ml of distilled water. The mixture was then subjected to sonication in a water bath for 1 hour. Subsequently, characterizations were conducted using UV-vis spectroscopy, FE-SEM, and EDS.

2.2.4 Photocatalysis experiments

Photodegradation of methylene blue (MB) was utilized to evaluate the photocatalytic activity of all samples, namely WO_{3-x}, SnO_2, and WO_{3-x}/SnO_2 composite. For measuring photocatalysis, these solvents were mixed with MB aqueous solution under constant magnetic stirring, then irradiated under 210 mW LED light with a UV cut filter (330 nm) at a 50 cm distance. The absorption readings were recorded for different times: dark time (-30 minutes), at zero min.,

and at 60 min. with 10 min. interval to investigate the gradual deterioration of MB by photodegradation.

2.3 Synthesis of WS_2/Go/Au

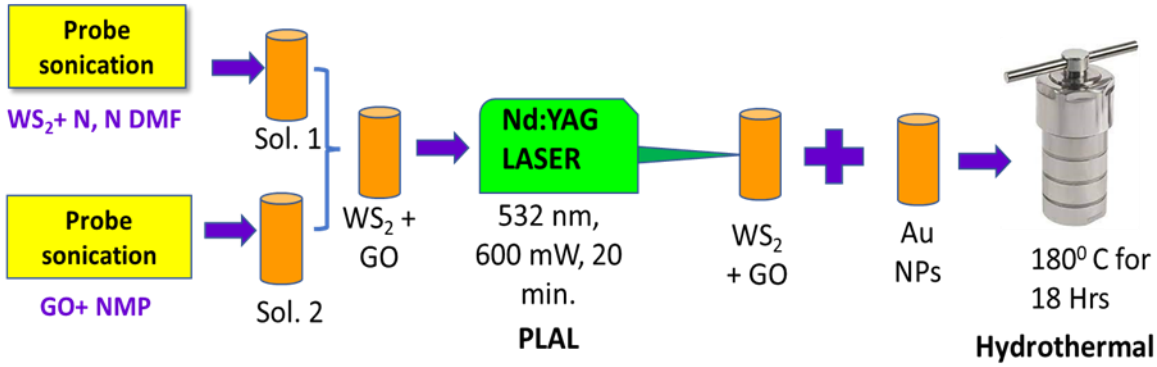

Fig. 6: Experimental setup for obtaining nanocomposites.

2.3.1 Preparation of WS_2

In this experiment, we have taken tungsten disulfide (WS_2) powder (10 mg) as a bulk material and mixed it in equal amounts of N, N-DMF (10 ml) followed by 10 minutes probe sonication using VIOLAMO Sonicstar 85 before ablating the prepared sample with ns laser ablation. The bulk WS_2 powder with an average sheet of 4-6 µm size was used for this experiment, and it was purchased from Sigma-Aldrich. Prepared sample exposed for 20 minutes. Before laser ablation, the solution underwent continual magnetic stirring and was irradiated using the second harmonic of a Nd:YAG laser (532 nm, repetition freq. 10 Hz, 600 mW, pulse width 10 ns). The ablated sample was characterized using UV-spectroscopy, FE-SEM, EDS, Raman, XRD, TEM-EDS.

2.3.2 Preparation of WS_2/GO

Here we used bulk WS_2 powder purchased from Sigma-Aldrich having sheet size around few micrometers with well synthesized graphene oxide prepared by hammers method taken in equal proportion and then tungsten disulfide (WS_2) powder (10 mg) mixed in an equal amount of N,N-DMF (10 ml) followed by 10 minutes probe sonication using VIOLAMO Sonicstar 85

prior to dropwise adding in second sample prepared by graphene oxide (GO) powder (10 mg) mixed it in an equal amount of NMP (10 ml) followed by 10 minutes probe sonication using VIOLAMO Sonicstar 85. After two samples were added completely, the prepared mixed was exposed to ns laser ablation with a solution that underwent continual magnetic stirring and irradiated with the second harmonic Nd:YAG laser (532 nm, repeating frequency 10 Hz, 600 mW, pulse width 10 ns). The ablated sample was characterized.

2.3.3 Preparation of WS_2/GO/Au

A very similar method as above was used to prepare the WS_2/GO mixed and then dropwise added Au solution prepared by laser ablation method by irradiating Au plate for 20 minutes in (40 ml) distilled water solution at 600 mW using 2nd harmonic of a Nd:YAG laser (532 nm, repeating frequency 10 Hz, pulse width 10 ns) using the hydrothermal method into WS_2/GO solution under continual stirring. After completing 30 min of stirring, the heterogenous solution was moved in the 100 mL Teflon lined autoclave and positioned in a furnace at 180° C for 18 h. After 18 hours, the autoclave was kept for a few more hours to get cooled down naturally at room temperature. The cooled sample was characterized using UV- vis spectroscopy, FE-SEM, EDS, Raman, XRD, TEM-EDS. A representative experimental setup is shown in Fig. 6.

2.3.4 Photocatalysis experiments

The prepared samples, including WS_2, WS_2/GO, and WS_2/GO/Au Composite, were put to the test to determine their photocatalytic activity. To do so, each solvent was mixed with an MB aqueous solution and stirred constantly. Then, this mixture was subjected to 300 mW LED light with a UV cut filter (330 nm) at a distance of 60 cm. Absorption readings were measured at 10 minutes intervals, starting from the dark time (-30 minutes) and continuing up to 80 minutes, to study the increasing photodegradation of MB.

Chapter 3: Tungsten suboxide petal-like nanosheets and Characterizations

3.1 FE-SEM and SEM-EDS analysis

Fig. 7 (a-e) provides a comprehensive visual representation of the morphological and structural transformations observed in bulk WS_2 and nanosecond (ns) laser-ablated WS_2 samples across four distinct ablation durations: 5, 10, 15, and 20 minutes. The scanning electron microscopy (SEM) images captured at each time point show variations in the changing characteristics of the material.

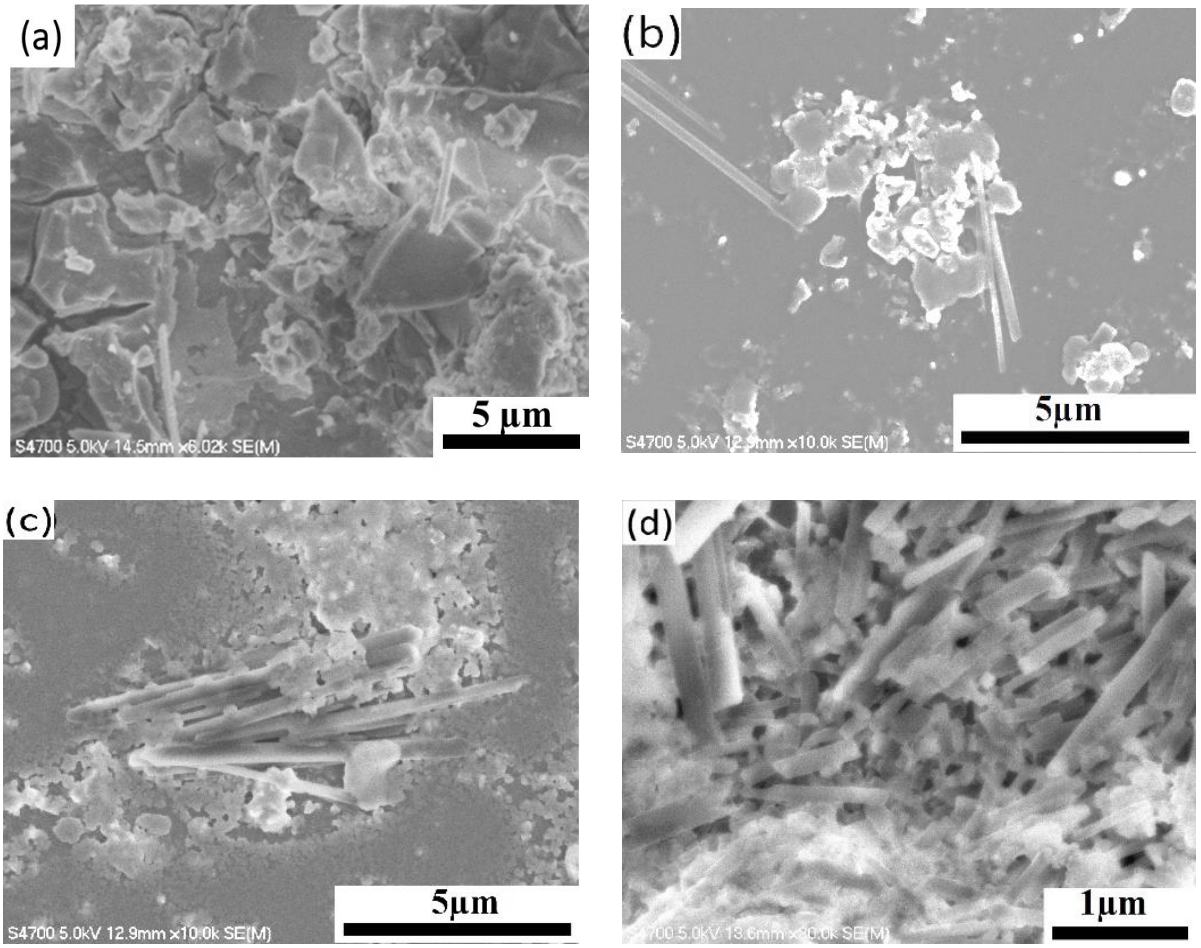

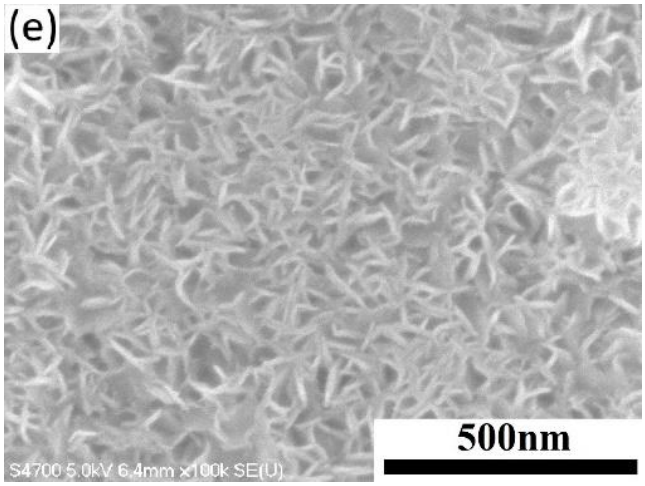

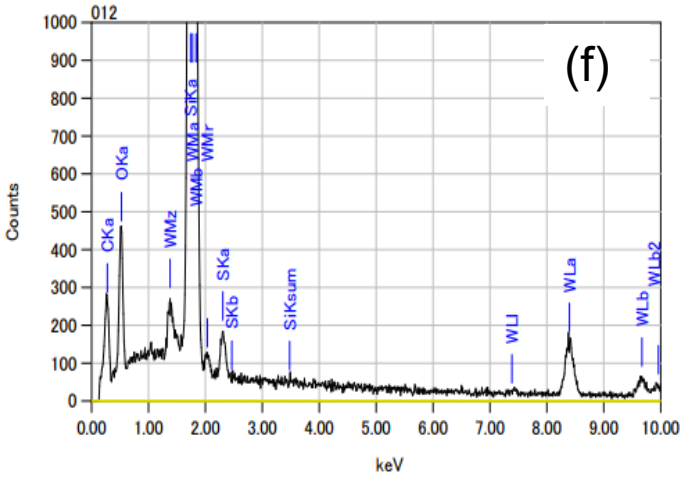

Quantitative analysis					
Element	(keV)	Mass %	σ	Atom %	K
C K	0.277	11.88	0.07	31.87	2.3237
O K	0.525	9.82	0.09	19.78	7.4865
Si K	1.739	34.14	0.05	39.18	44.9817
S K*	2.307	1.72	0.07	1.73	1.6205
W M*	1.774	42.44	0.2	7.12	43.5876
Total		100		100	

Fig.7. SEM images (a) bulk WS_2, (b) 5 min, (c) 10 min, (d) 15 min, (e) 20 min laser ablated WS_2 (f) EDS spectrum of WO_{3-x}.

The sequence of SEM images shows the gradual transition from the initial state of bulk WS_2 to the altered state induced by the ns laser ablation process. We observe the presence of relatively large sheets, measuring a few micrometers in size initially. As the laser ablation duration increases, a transformation in sheet size is observed. After 20 minutes of laser ablation,

the substantial sheets convert into finely structured, uniform nanosheets with dimensions in the range of 10-20 nanometers. This change in the formation of petal-like nanosheet structures strongly indicates the power of nanosecond laser energy and the length of the ablation process.

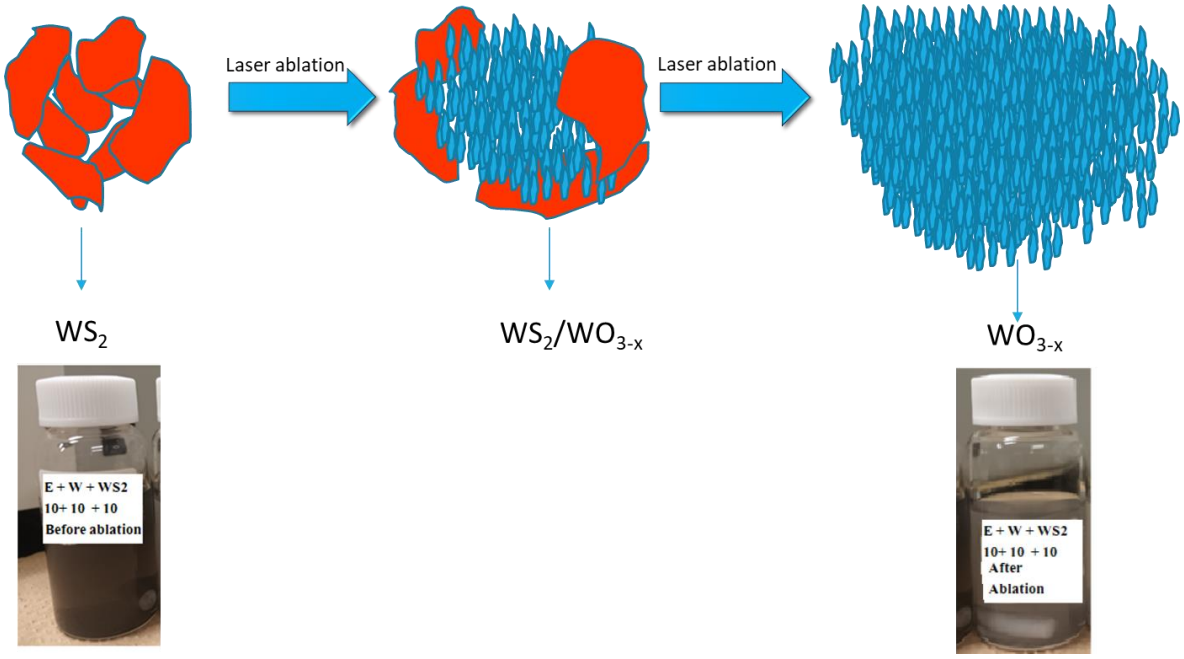

Fig. 8. Schematic representation for formation of WO_{3-x}

It becomes clear that the WS_2 material is efficiently refined and restructured over time by the interaction of the intense laser pulses. This controlled and methodical progression from microsheets to nanosheets resulted in the appearance of these nano petal-like sheets, which sheds light on the significant influence of laser energy and ablation time on the material's shape and structure. In conclusion, Fig. 8 shows the schematic representation of dynamic changes that bulk WS_2 underwent during ns laser ablation to form WO_{3-x}. It emphasizes the progressive transition from bigger micro sheets to the precisely made and homogeneous petal-like nanosheets that were attained after 20 minutes of laser treatment. This change emphasizes the crucial role that laser energy and ablation time played in determining the final nanoscale structure of WS_2.

Fig. 7 (f) shows the EDS spectrum, which indicates that WO_{3-x} was formed after 20 minutes of laser treatment. The EDS spectrum shows that WO_{3-x}, where x is 0.23, is present ($0 < x < 0.4$). The table values in Fig. 7 (f) suffice the above result.

3.2 XRD analysis

The X-ray diffraction (XRD) patterns shown in Fig. 9 correspond to a) WS_2 in its bulk form and b) WO_{3-x}. When comparing bulk WS_2 to laser ablation, noticeable changes occur in many peculiar peaks, either causing them to disappear or shift, which suggests the creation of nanostructures.

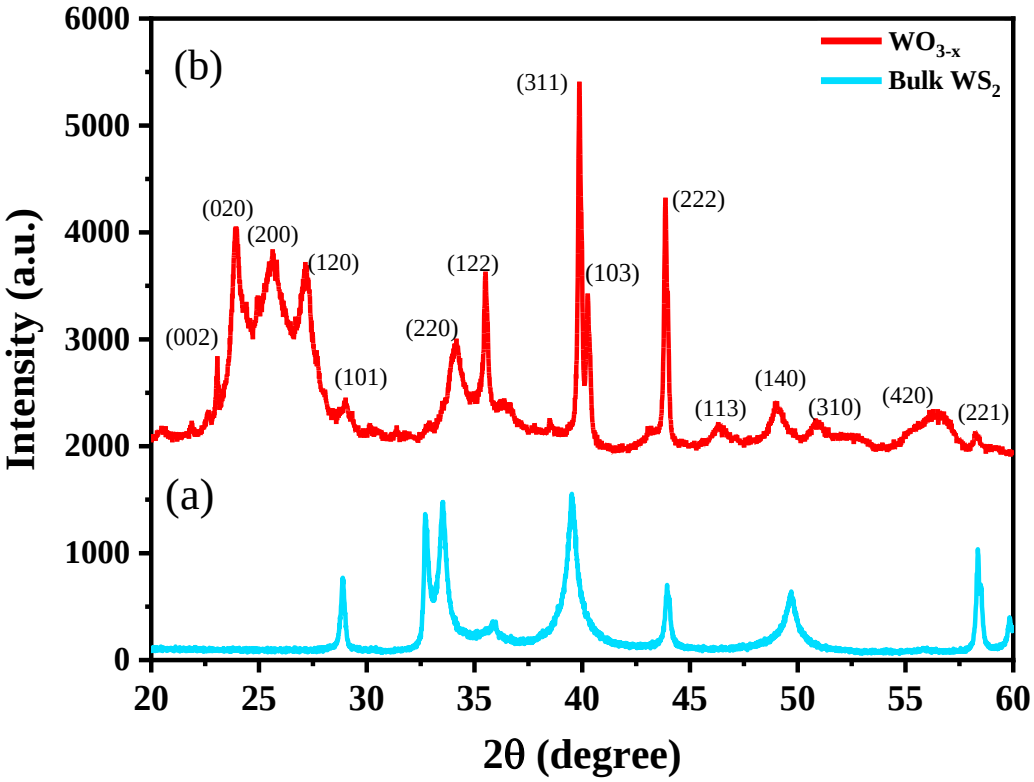

Fig. 9. XRD spectra of bulk a) WS_2 and b) WO_{3-x}

The synthesized powder exhibits a different pattern than bulk WS_2, and this difference corresponds to the number, location, and intensity of the produced peaks. The blue powder of WO_{3-x} exhibited distinct and strong peaks, indicating the presence of a polycrystalline structure.

The observed peaks match the crystal structure and phase indicated by the JCPDS data files 04-007-2322, 08-0237, 72-1465, and 20-1324 [62]. The observation indicates a strong correlation between the peaks, revealing a hexagonal structure of WO_3. Other peaks may be attributed to various WO_{3-x} phases, confirming the pristine hexagonal structure of the produced blue WO_{3-x} powder [63]. Distinct and identifiable diffraction peaks have been identified at specific angles of 2θ = 23.04°, 23.8°, 25.1°, 27.1°, 28.96°, 34.16°, 35.51°, 39.82°, 40.43°, 43.86°, 46.34°, 49.03°, 50.87°, 56.45°, and 58.28°. These peaks correspond to the crystallographic planes (002), (020), (200), (120), (101), (220), (122), (311), (103), (222), (113), (140), (310), (420), and (221) of the suboxide phase of WO_{3-x}.

3.3. UV-vis analysis

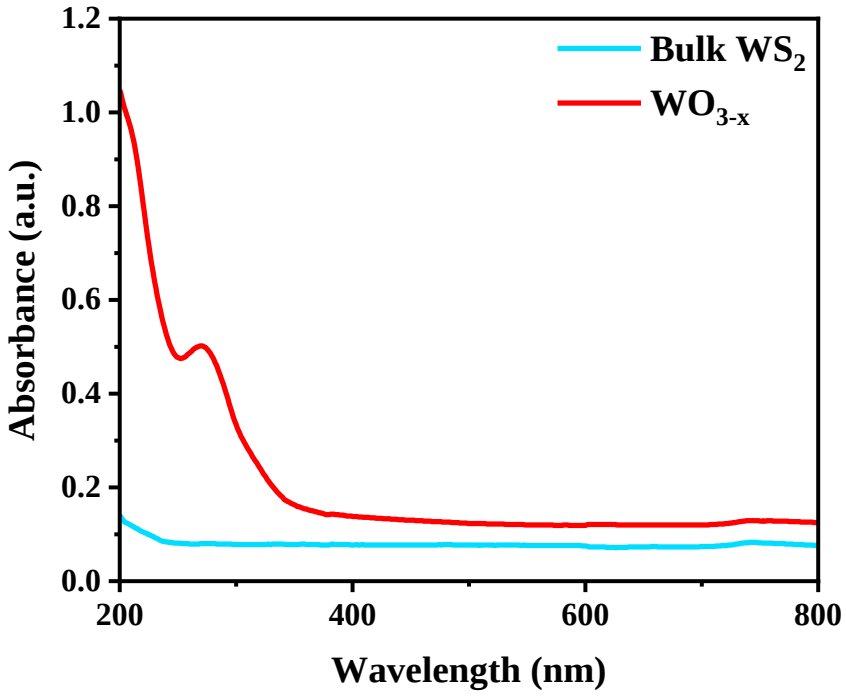

Fig. 10. UV-visible spectra of bulk WS_2 and WO_{3-x}

Fig. 10 illustrates the UV-vis spectra of bulk WS_2 and WO_{3-x}. The presence of a hump-like structure is seen at about 270 nm, indicating that the bulk WS_2 underwent a transformation into sub-oxide tungsten oxide (WO_{3-x}) [64]. One possible explanation for the observed rise in absorption after ablation is the exfoliation of the WS_2 microsheet into petal like nanosheets.

3.4 Raman analysis

In Fig. 11, we can see the Raman spectra of WO_{3-x} powder, which exhibit the expected A_{1g} and E^1_{2g} modes. There are four distinct peaks in the raman spectrum of WO_{3-x}, corresponding to 268 cm^{-1}, 326 cm^{-1}, 707 cm^{-1}, and 807 cm^{-1}. The W-O-W stretching vibration mode is responsible for the peaks at 707 cm^{-1} and 807 cm^{-1}, whereas the two lower peaks at 268 cm^{-1} and 326 cm^{-1} are associated with the W-O-W bending mode vibration (O-W-O) [65].

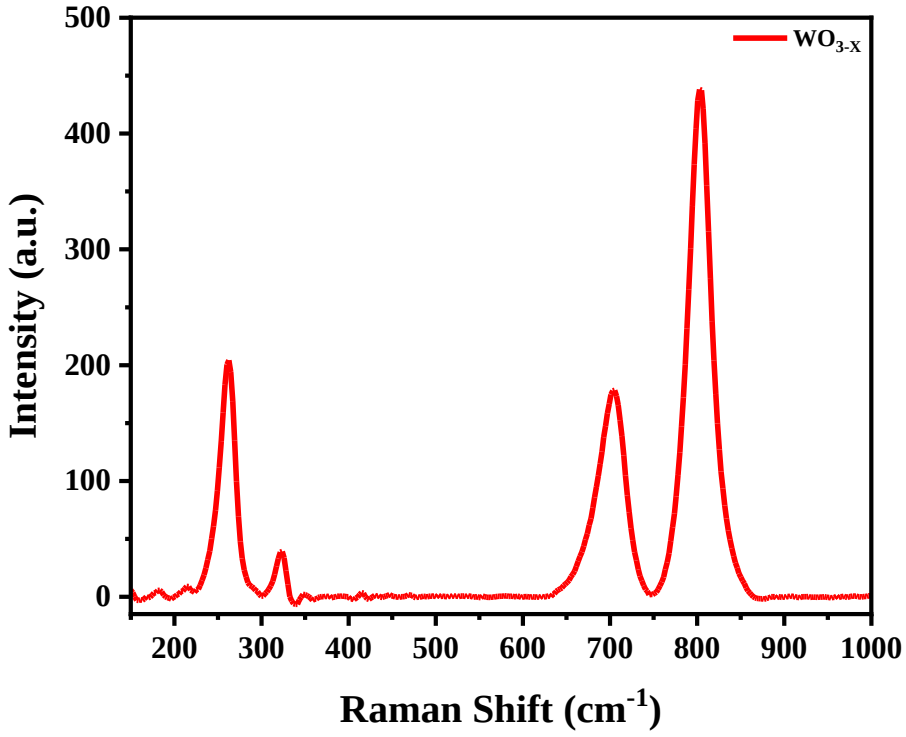

Fig. 11. Raman spectrum of WO_{3-x}

Chapter 4: WO_{3-x}/ SnO_2 synthesized by laser ablation method and its characterization.

4.1 UV-vis analysis

Fig. 12 is UV-vis spectra of WO_{3-x} sub-oxide, SnO_2, and the mixed composite of WO_{3-x}/SnO_2. Semiconductors were used in optoelectronic materials due to their remarkable optical characteristics [66]. The minor hump structure in the tungsten suboxide spectra was located at around 270 nm, indicating that the bulk WS_2 was changed into (WO_{3-x}) tungsten sub-oxide [67]. The exfoliation of tungsten disulfide microsheets in nanopetals is shown by a spike in absorbance upon ablation. The crystalline formation of as-synthesized SnO_2 was indicated by the broad and intense absorbance that the SnO_2 nanocrystals displayed around 247 nm [68]. The binary composite WO_{3-x}/SnO_2 UV-vis revealed structureless light absorption in visible or nearly visible areas, indicating that the prepared composite material had photocatalytic properties. [69].

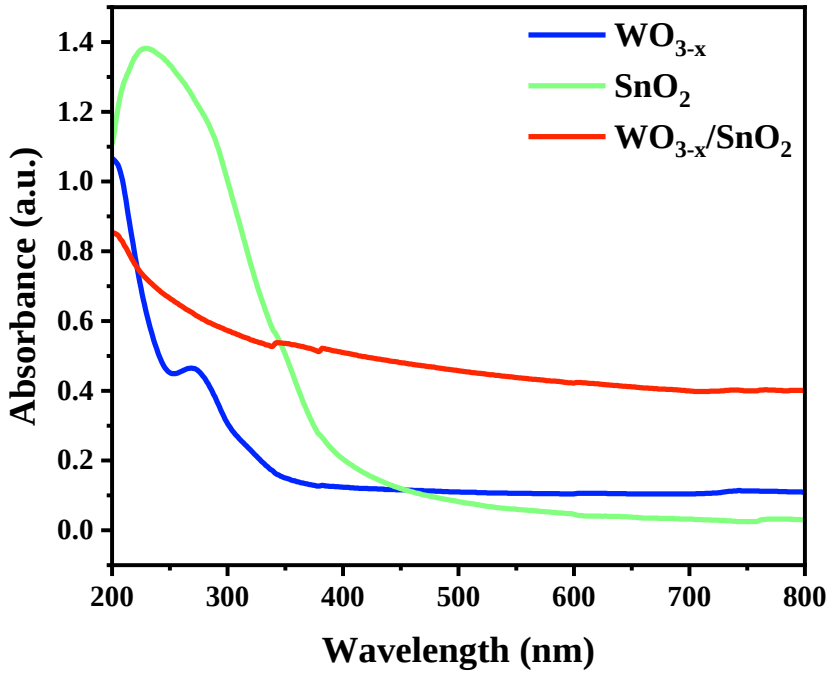

Fig. 12. UV-visible spectra of WO_{3-x}, SnO_2 and WO_{3-x}/SnO_2

4.2 FE-SEM analysis

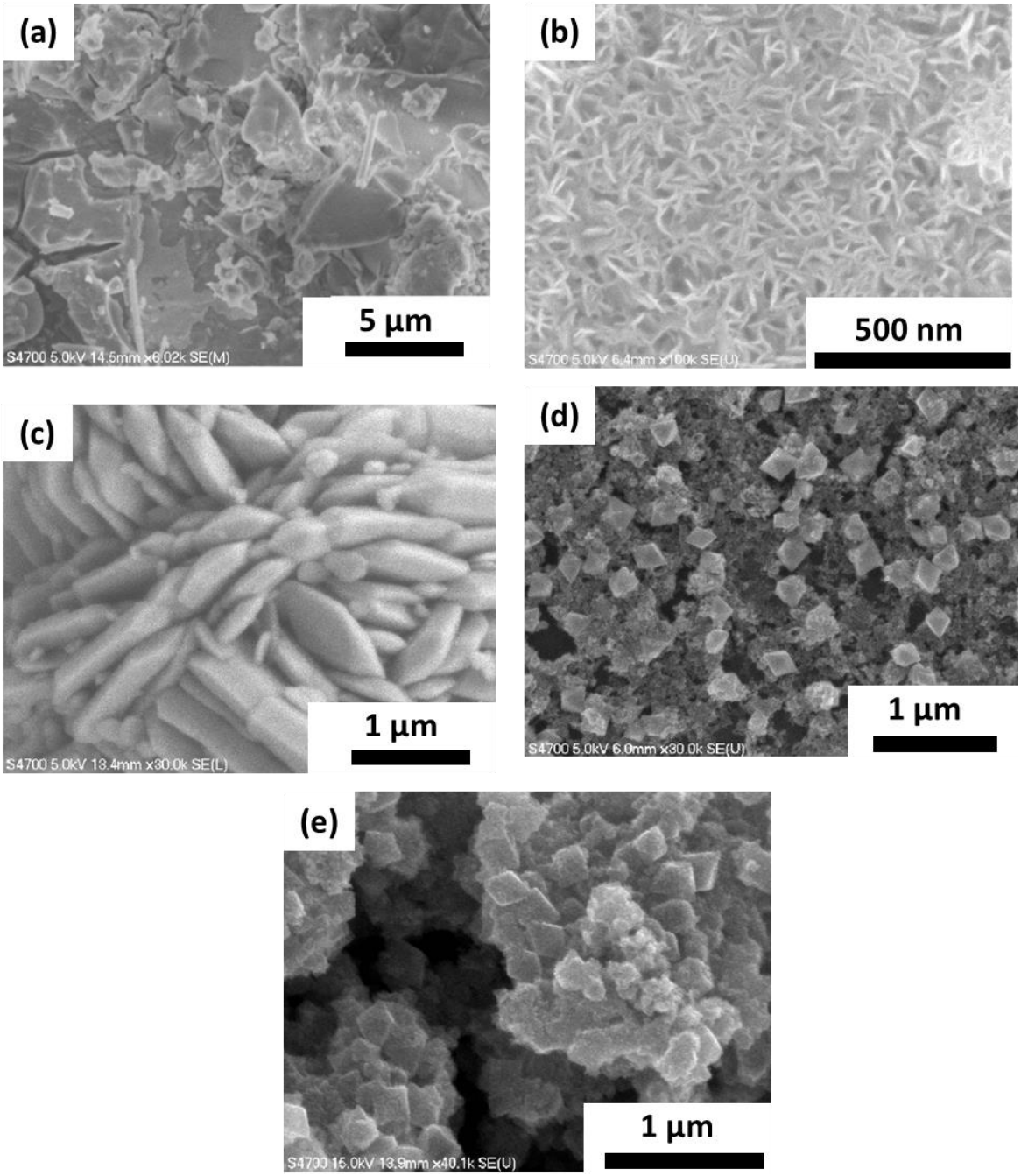

Fig. 13. FE SEM images of a) bulk WS_2 b) WO_{3-x} c) bulk SnO d) SnO_2 e) WO_{3-x}/SnO_2

As seen in Fig. 13, FE SEM images of a) bulk $WS_{2,}$ b) $WO_{3-x,}$ c) bulk SnO, d) ablated SnO_2, and e) WO_{3-x}/SnO_2 reveal the noticeable difference in morphological structures for all the prepared samples. Fig. 13 (a) shows a few micrometer sheets of bulk WS_2, and Fig. 13 (b)

illustrates the formation of the WO_{3-x} with a petal-like morphology and uniformly distributed structure covering over 70% region. The bulk SnO has crystalline nature that shows agglomeration with the size of ~1µm sheets in demonstrated in Fig. 13 (c). After ablation, the extremely well-grown and crystalline form of SnO_2 octahedron shape, with diameters ranging from 100 nm to 150 nm, is shown in Fig. 13(d). Since octahedral crystals always have a greater crystal field stabilization energy than tetrahedral crystals, the creation of six links is preferable to four [70]. Fig.13 (e) of binary composite shows well-mixed with keeping morphologies intact in WO_{3-x}/SnO_2, suggesting the intact properties will complement each other for improved photocatalytic properties.

4.3 EDS analysis

Fig. 14 (a) shows the EDS spectrum of bulk WS_2. This spectrum can be used to identify the chemical elements present in the sample. Fig. 14 (b), elemental mapping is employed to visually represent the formation of WO_{3-x} after applying nanosecond (ns) laser ablation to the WS_2 material. The graph in Fig. 14 (b) illustrates the distribution of tungsten suboxide (WO_{3-x}) throughout the sample. It is noteworthy that the value of x falls between 0 and 0.4, with a specific value of x being 0.22. This study verifies the growth of tungsten suboxide in the material because of the ns laser ablation process. Fig. 14 (c) explores the EDS spectrum of bulk SnO, yielding similar spectrum features for this material. Fig. 14 (d) provides information on the elemental composition of the SnO_2 octahedron crystal structure. The EDS spectrum shown in Fig. 14 (d) confirms that the octahedron nanocrystals contain mostly tin and oxygen, as indicated by the prominent peaks corresponding to these elements. These two prevailing peaks, without any notable peaks from other elements, suggest that the SnO_2 powder was produced in its pure form. Fig. 14 (e) presents a detailed summary of element composition of WO_{3-x}/SnO_2 composite material. The spectrum provides confirmation of the presence of all associated components, therefore ensuring the composite nature of this material.

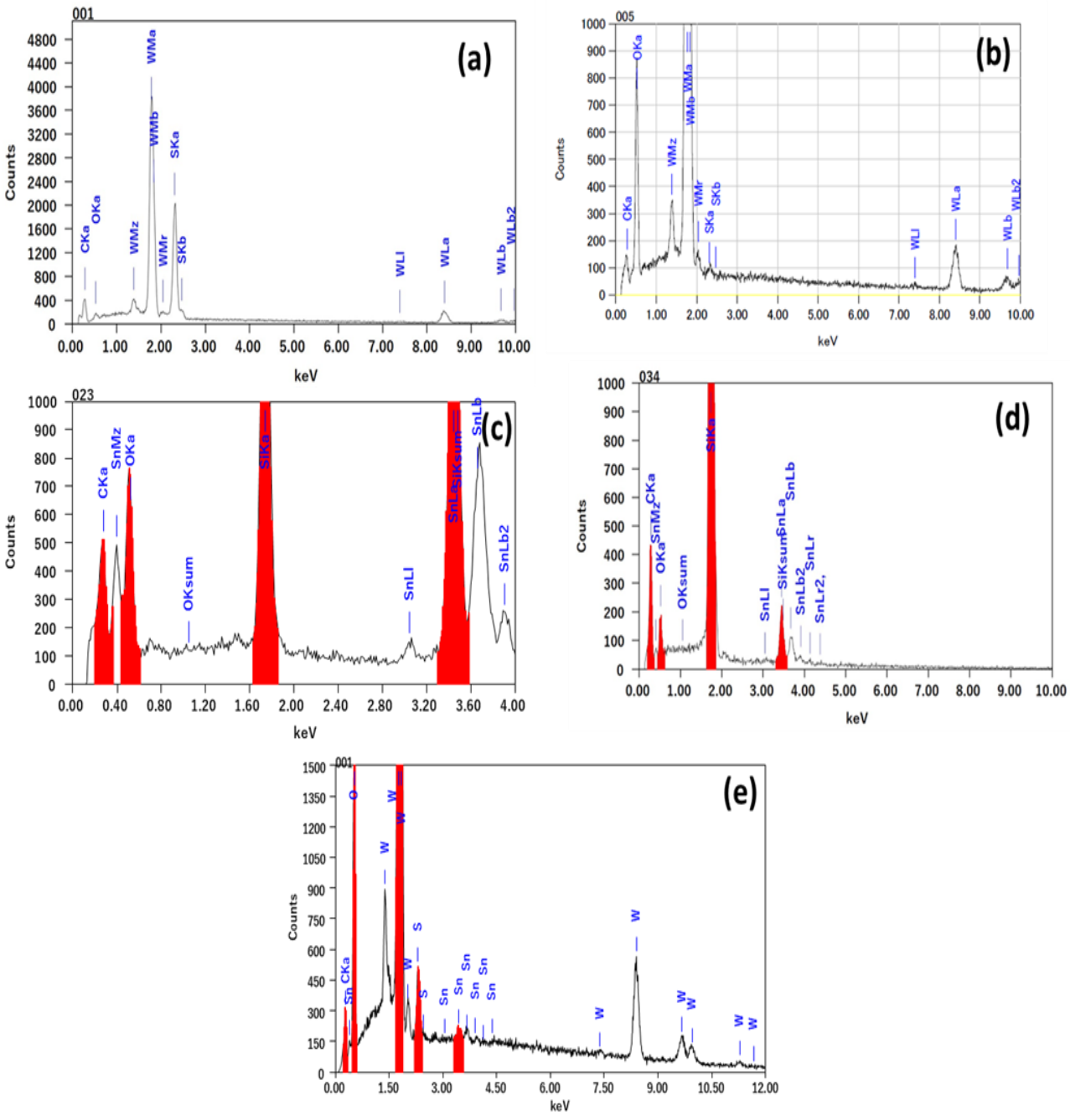

Fig. 14. EDS spectra of a) bulk WS_2 b) WO_{3-x} c) bulk SnO d) SnO_2 and e) WO_{3-x}/SnO_2

4.4 XRD analysis

XRD pattern of WO_{3-x}/SnO_2 binary nanocomposite is displayed in Fig. 15. Sharp diffraction peaks will vividly imply the octahedron crystals and nanopetal like flake structures of the produced composite. The WO_{3-x} nanopetal like flake structure (JCPDS card No. 33-1387) and the SnO_2 octahedron crystal (JCPDS card No. 41-1445) [71] both display diffraction peaks for composite [71]. The production of SnO_2 octahedron crystals is revealed by the XRD peaks at 2θ values of 26.940, 33.350, 37.540, and 52.080. Furthermore, XRD peaks at 2θ values of 57.730, 51.240, 34.50, and 30.260 show that WO_{3-x} forms a nanopetls like flake structure [72].

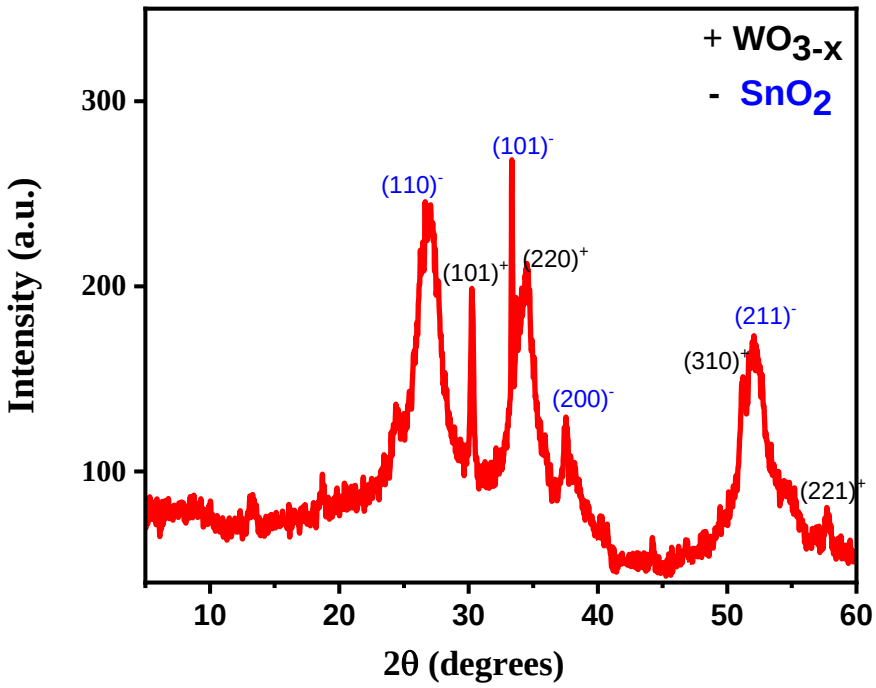

Fig. 15. XRD spectrum of WO_{3-x}/SnO_2 composites

4.5 Reduction of methylene blue and efficiency of photocatalytic reduction

UV spectroscopy was used to measure the photocatalytic performance, and the resulting absorption spectra for the degradation of MB were shown in Fig. 16 (a-c) for WO_{3-x} nanopetals, SnO_2 octahedron crystals, and WO_{3-x}/SnO_2 composite, respectively.

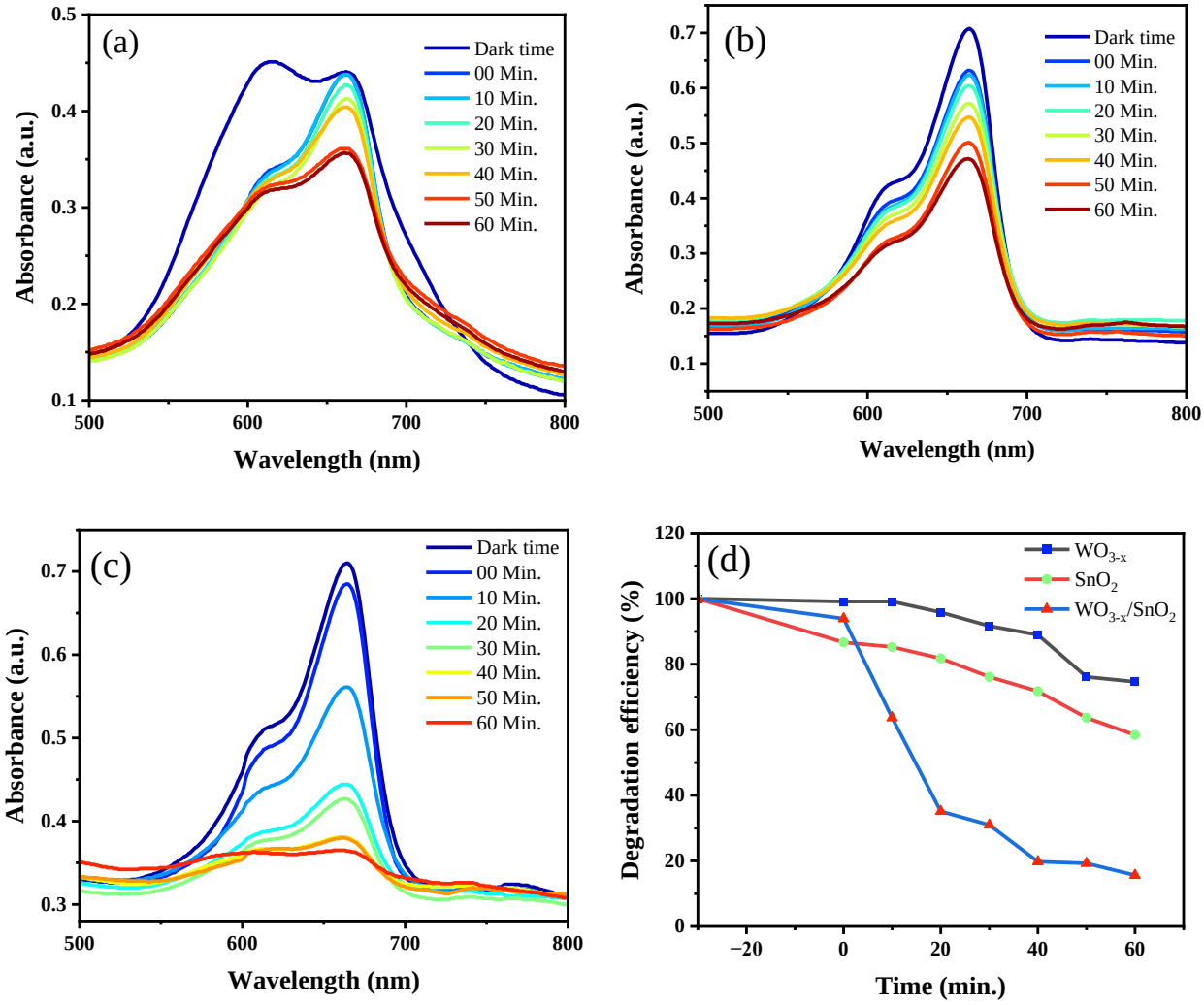

Fig. 16. UV–vis spectra of (a) WO_{3-x} (b) SnO_2 octahedron crystals and (c) WO_{3-x}/SnO_2 binary composite regarding the photocatalytic degradation of MB also (d) degradation efficiency in percentages of WO_{3-x}, SnO_2, and WO_{3-x}/SnO_2

As shown in Fig. 16, various materials employed have an impact on MB efficiency of deterioration when exposed to UV-vis light (> 330 nm). The following formula was used to determine photodegradation efficiency of each material:

$$\textit{Degradation efficiency}\ (\%) = (A_0 - A_t / A_0) * 100\ \%$$

Here A_0 and A_t denote MB absorption intensity at time zero and 60 min., respectively.

As shown in Fig. 16(b), the as-synthesised SnO_2 octahedron crystals showed a degradation efficiency of 41.6% after 60 minutes. Comparatively, during the same 60 minutes, the WO_{3-x}

nanopetal-like structure in Figure 16(a) had a degradation efficiency of 25.4%. According to Fig. 16(c), the degrading efficiency of the binary compound WO_{3-x}/SnO_2 is 84.4%. When compared to tungsten suboxide and SnO_2 in their raw forms, the binary compound that was created has superior degradation potential. The graphical and comparative depiction of the degrading efficiency of prepared samples is presented in Fig. 16(d). Various factors, such as band gap characteristics, nanopetals or crystals, morphological structure, photochemical stability, and crystal defect, can result in different levels of photocatalytic activity [73].

When dye molecules are exposed to airborne oxygen and ultraviolet light from the sun, they spontaneously decompose [74–75]. By using a semiconductor material as a photocatalyst, we can accelerate this normally slow deteriorating process. Analogous research has demonstrated that semiconductor materials demonstrated negligible photocatalytic dye degradation during the dark phase. It is common practice to employ heterogeneous photocatalysis to break down hazardous molecules. This implies that the necessary energy from light is absorbed by materials such as WO_{3-x}/SnO_2. The photocatalytic material's electrons migrate from its valence band (VB) to its conduction band (CB) because of light energy absorbed by the exposed substance. In response, a responsive pair of electrons and holes forms, transporting in the direction of the water-semiconductor interface, the point at which electrons are exchanged between adjacent species. Contaminants are thus eliminated from the medium as a result of this interaction [76]. This result thus supports the finding that photocatalytic degradation is almost exclusively dependent on light [77].

Chapter 5: Photocatalytic activity of WS_2/GO/Au nano-composites

5.1 UV-vis analysis

Among many types of efficient analytical techniques, UV-vis spectroscopy is one that is utilized to determine the electronic properties of materials. In this section, we present the UV-vis spectra of WS_2, WS_2/GO, and WS_2/GO/Au composite materials as measured from U-2010 (Hitachi, Japan). The composite materials WS_2, WS_2/GO, and WS_2/GO/Au were created and evaluated using UV-vis spectroscopy in the 200-800 nm range after synthesis.

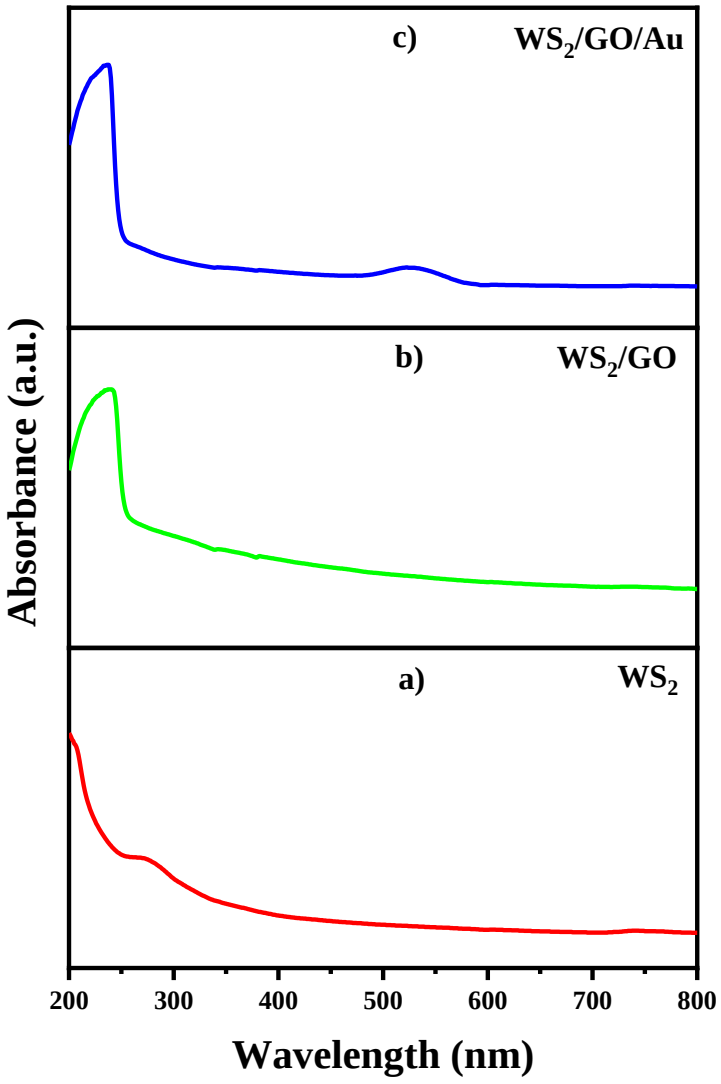

Fig. 17. UV-vis spectra of a) WS_2 b) WS_2/GO c) WS_2/GO/Au

The UV-vis spectra of the WS_2, WS_2/GO, and WS_2/GO/Au composite materials are shown in Fig. 17. Referring to Figure 17 (a-c), the presence of a distinct peak with a slight hump at around 280 nm was seen in all three materials, indicating the presence of nanocrystalline thin films low sulfur [78]. Fig. 17 (b-c) shows that the WS_2/GO and WS_2/GO/Au composite materials have an additional peak at about 233 nm, which appears due to the π -π^* transition of the C-C bonds in the GO layer [79]. The absence of this peak in the spectra of pure WS_2 implies GO has been successfully incorporated into the composite material. In addition, the composite material comprised of WS_2/GO/Au exhibits an additional peak at about 537 nm in Fig. 17 (c). This peak is attributed to the surface plasmon resonance (SPR) of the Au nanoparticles [80]. The appearance of this peak denotes the successful incorporation of Au nanoparticles into the composite material. The intensity of the surface plasmon resonance (SPR) peak is directly proportional to the size and amount of the Au nanoparticles. Hence, the higher intensity of the SPR peak seen in the spectrum of the WS_2/GO/Au composite material, in comparison to the WS_2/GO composite material, suggests the efficient incorporation of more of the amount of Au nanoparticles. The outcomes of the UV-vis spectroscopy analysis demonstrate that the WS_2, WS_2/GO, and WS_2/GO/Au composite materials were successfully synthesized and characterized. The appearance of additional peaks in the spectra of the composite materials confirmed the incorporation of GO and Au nanoparticles into the WS_2 layer. Also, the relationship between the intensity of the SPR peak in spectra and the size and concentration of the Au nanoparticles was observed.

5.2 FE-SEM analysis

Field emission scanning electron microscopy (FE-SEM) is an efficient method of analysis used for studying the surface structure and elemental composition of materials. In this report, we

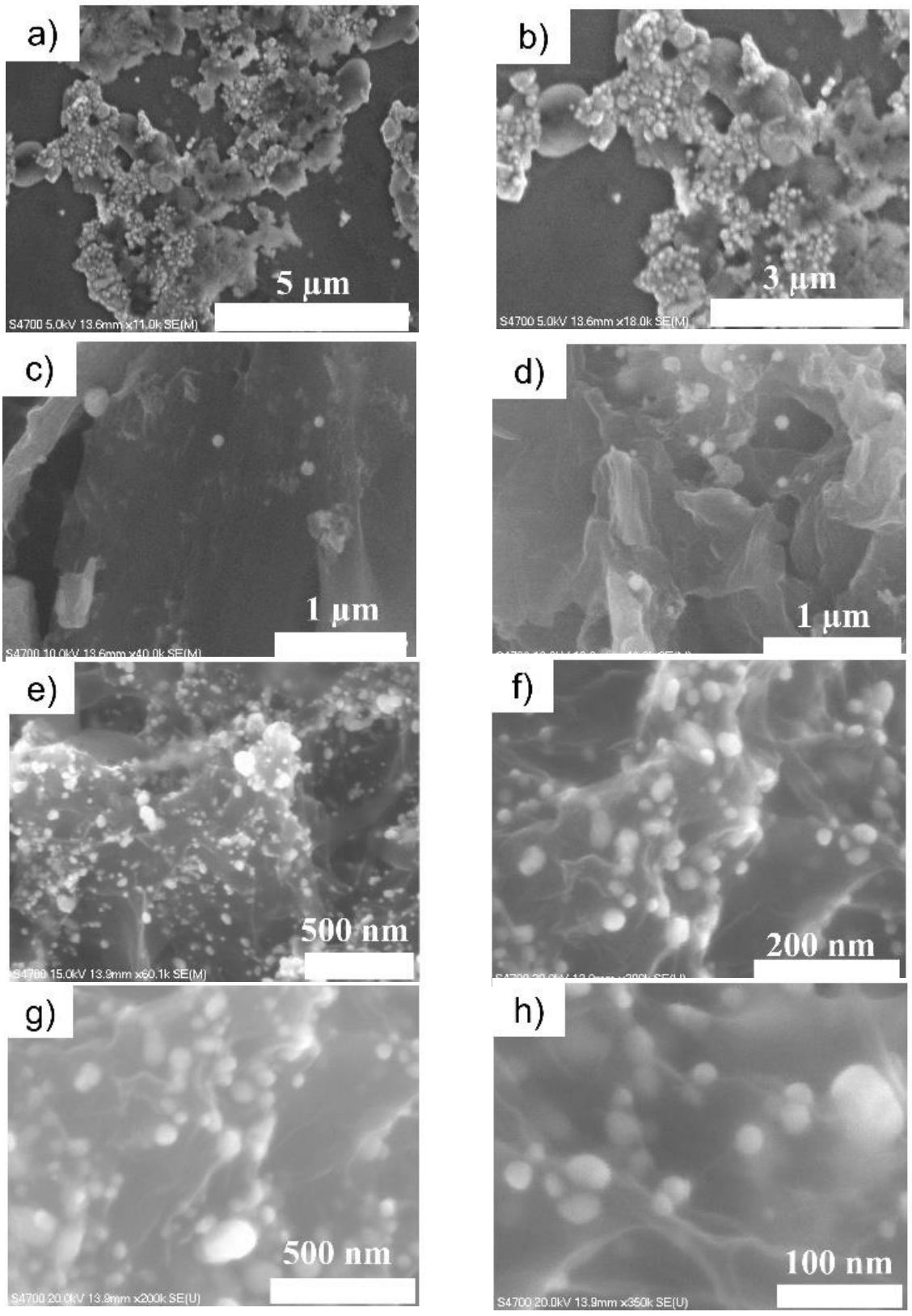

Fig. 18. FE-SEM images of (a, b) WS_2, (c,d) WS_2/GO and (e- h) WS_2/GO/Au

provide the results of research analyzing the FE-SEM images of WS_2, WS_2/GO, and WS_2/GO/Au composite materials. The synthesis of the WS_2, WS_2/GO, and WS_2/GO/Au composite materials was carried out by a laser ablation and hydrothermal technique. The materials were then examined using FE-SEM microscopy utilizing with an accelerating voltage ranging from 5 to 20 kV. Fig. 18 (a-h) displays the FE-SEM images of WS_2, WS_2/GO, and WS_2/GO/Au composite materials. Fig. 18 (a-b) illustrates synthesized WS_2 material with nanometer-sized, extremely small, circular clusters of bright white tungsten spread throughout the films [78]. Next, WS_2 nanosheets appear to be spread at random across the surface of GO sheets in the WS_2/GO composite material (Fig. 18 (c-d)), which indicates that GO has been successfully incorporated into the composite. SEM images of ternary materials shown in Fig. 18(e-h) reveal the existence of WS_2 nanosheets, which typically measure around 500 nm in size. Moreover, as can be seen in Figure 18 (g-h), the WS_2/GO/Au composite material reveals the presence of Au nanoparticles with average size of 20-30 nm on the surface of the WS_2 nanosheets. The Au nanoparticles exhibit a uniform distribution on the surface of WS_2 nanosheets, suggesting the successful incorporation of the Au nanoparticles into the composite material. The occurrence of Au nanoparticles in the WS_2/GO/Au composite material has also been demonstrated using energy-dispersive X-ray spectroscopy (EDS). The EDS analysis confirmed the efficient incorporation of Au nanoparticles into the WS_2/GO/Au composite material by identifying the presence of Au peaks in the spectrum. The FE-SEM findings demonstrate the effective synthesis and characterization of WS_2, WS_2/GO, and WS_2/GO/Au composite materials. FE-SEM imaging and EDS analysis both revealed that the composite material consisted of WS_2 nanosheets with an average size of around 500 nm. Additionally, the GO and Au nanoparticles were successfully incorporated into the material.

5.3 SEM-EDS analysis

SEM with EDS is a fundamental analytical technique employed for evaluating the surface structure and chemical composition of materials.

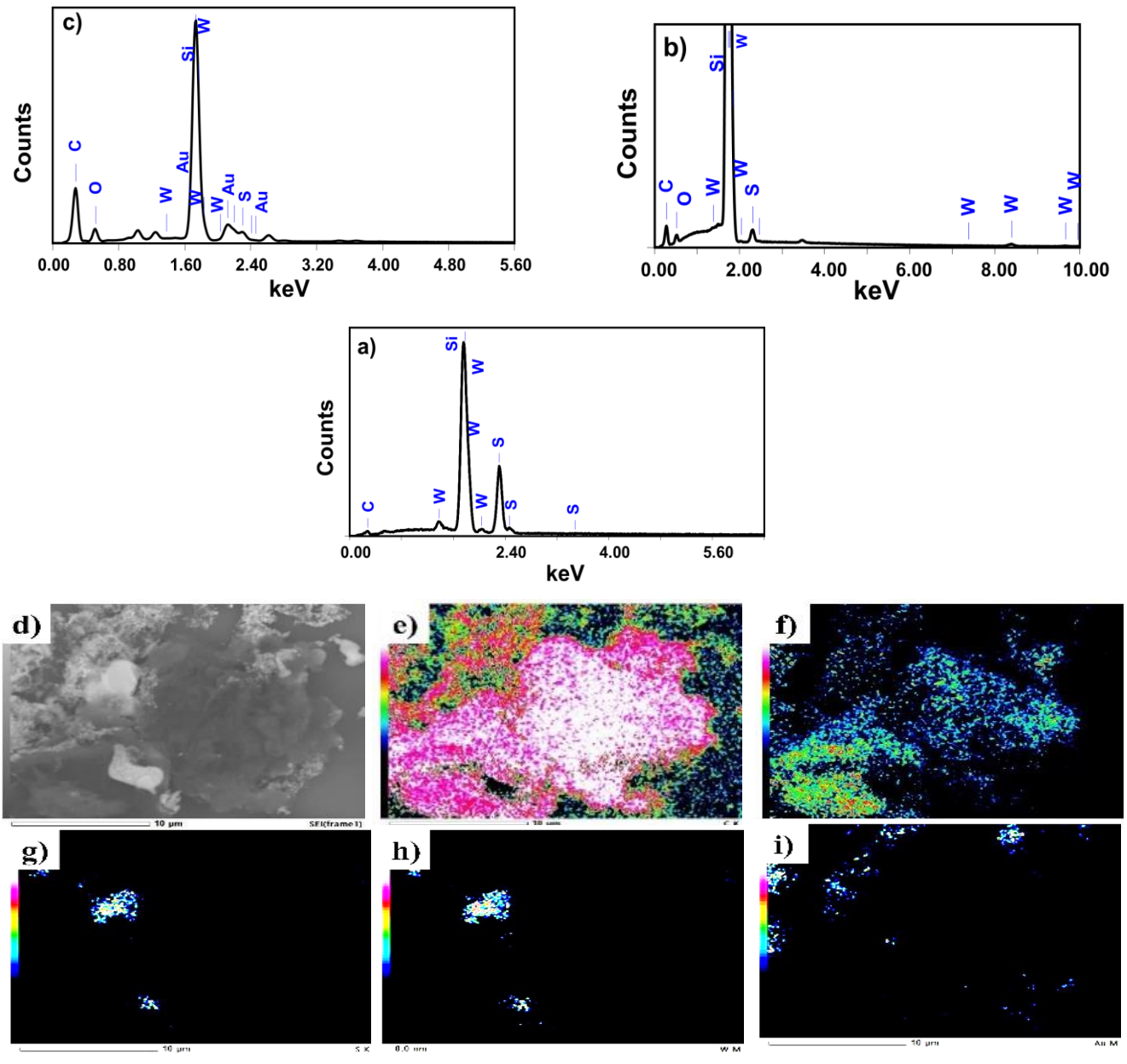

Fig. 19. (a) SEM-EDS spectra of WS_2, (b) WS_2/GO, (c) WS_2/GO/Au and (d, e, f, g, h, i) elemental mapping of WS_2/GO/Au composite.

Here, we discussed the outcome of the SEM-EDS analysis of WS_2, WS_2/GO, and WS_2/GO/Au composite materials. The WS_2, WS_2/GO, and WS_2/GO/Au composite materials were produced

by a laser ablation and hydrothermal technique. Then, the materials were analyzed using SEM-EDS analysis at an accelerating voltage of 15 kV. The EDS spectra of composite materials are displayed in Fig. 19 (a-c). EDS analysis of the synthesized WS_2 material, as shown in Fig.19 (a), revealed the presence of W and S components. The presence of W, S, C, and O elements in the WS_2/GO composite material was confirmed by EDS analysis as depicted in Fig. 19 (b). This provides evidence that the incorporation of GO into the composite material was successful. Also, as seen in Fig. 19 (c), the EDS analysis of the WS_2/GO/Au composite material confirmed the presence of Au peaks in addition to W, S, C, and O elements. The SEM-EDS images of the WS_2/GO/Au composite materials are shown with the help of Fig. 19 (d-i). The presence of Au peaks demonstrated that Au nanoparticles had been successfully incorporated into the composite material. Finally, the SEM-EDS findings show that the WS_2, WS_2/GO, and WS_2/GO/Au composite materials can be produced effectively and characterized. SEM imaging and EDS analysis were used to confirm the appearance of WS_2 nanosheets, the successful incorporation of GO and Au nanoparticles into the composite material, and the elemental composition of the composite materials.

5.4 XRD analysis

Fig. 20 (a) illustrates the XRD pattern of WS_2. The XRD pattern of WS_2 reveals that three different peaks at $2\theta = 14.75^{O}$, 29.32^{O}, and 44.37^{O} corresponds to the (002), (004), and (006) crystal planes of WS_2, respectively (JCPDS #08-0237). These peaks suggest that there is evidence of a layered structure; however, the peak at 14.75^{O} is considerably stronger than the other two peaks, confirming the presence of monolayered or very few layer structures [81-82]. The XRD pattern of GO is depicted in Fig. 20 (b). The XRD pattern of GO reveals the prominent peaks at $2\theta = 10.6^{O}$ and a minor peak at 42.4^{O}. The peak at 10.6^{O} represents the (001) plane and the peak at 42.4^{O} belongs to the (004) plane of GO, which leads to the stacking of graphene layers [83].

The (004) plane is also responsive to variations in interlayer spacing and the degree of graphene oxidation [84].

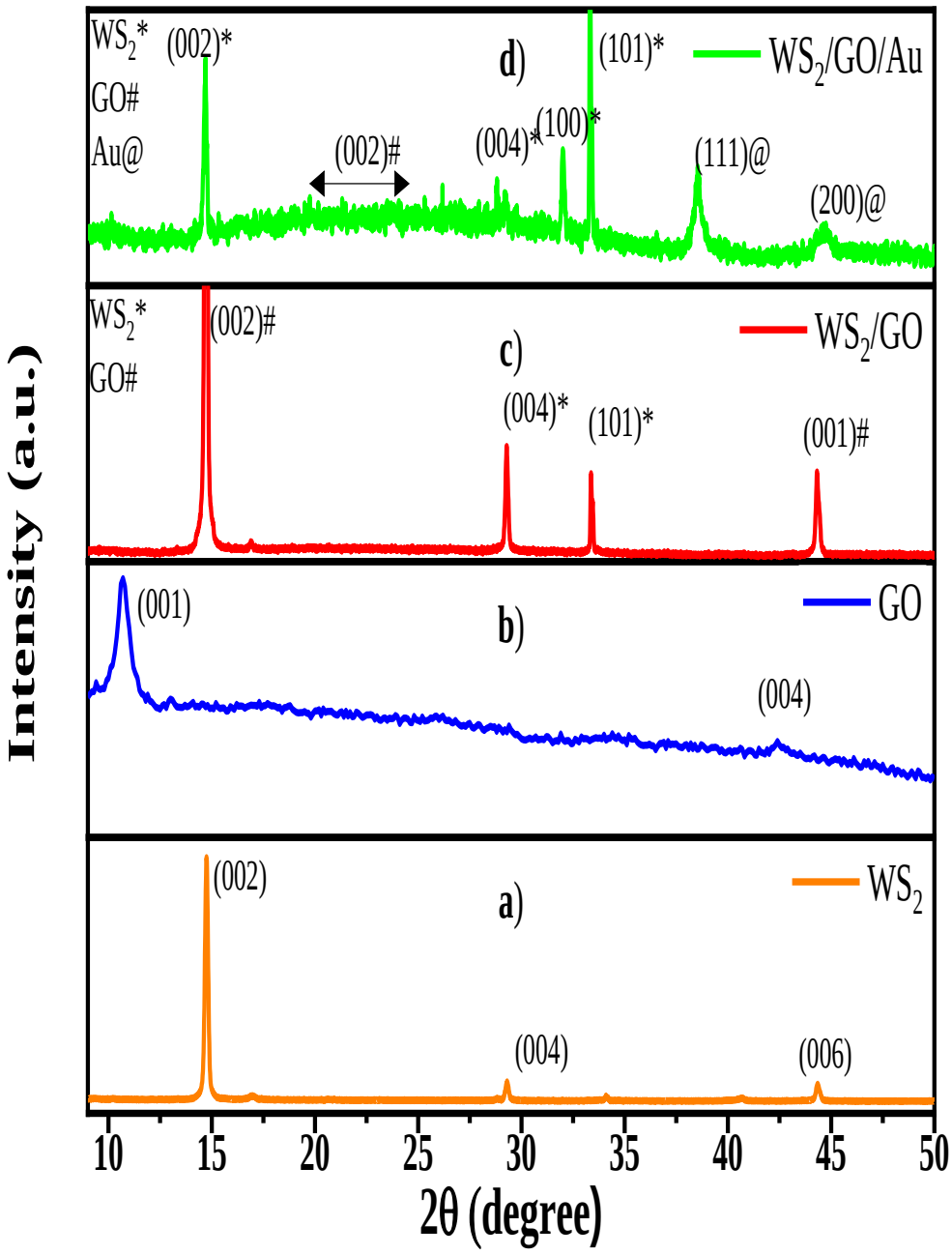

Fig. 20. (a) XRD spectra of WS_2, (b) GO, (c) WS_2/GO, (d) WS_2/GO/Au composite.

The XRD pattern of WS_2/GO binary composite obtained from Fig. 20 (c) exhibits various peaks, which suggest the presence of both WS_2 and GO in the composite material. The diffraction peaks at $2\theta = 14.95^{O}$, 29.01^{O}, and 33.49^{O} with respect to the crystal planes (002), (004), and

(101) of WS_2, respectively. These peaks are characteristic of layered transition metal dichalcogenides such as WS_2 and identified by the JCPDS file 08-0237 [81]. Their presence serves as evidence for the crystalline structure of the WS_2 nanosheets in the composite material. Furthermore, a broad hump is seen in the XRD pattern at about $2\theta = 44.32^{O}$. This peak is ascribed to the turbostratic band of disordered carbon materials. It is probable because of the presence of GO in the composite material. This peak indicates that the GO sheets in the composite material are not completely ordered and may be partially reduced or functionalized. Overall, the XRD pattern of the WS_2/GO binary composite clearly demonstrates the presence of both WS_2 and GO in composite material. It means GO sheets may have been transformed or modified during the synthesis process [85].

Fig. 20 (d) shows the XRD pattern of the ternary composite. The presence of diffraction peaks at $2\theta = 38.54°$ and 44.76°, which correspond to the (111), and (200) planes, respectively, provides the confirmation of the crystalline nature of AuNPs [86]. The diffraction peaks clearly indicate the presence of well-ordered AuNPs with a cubic crystal structure, including a face centered on the composite material. The noticeable hump near 22°- 24° represents the transformation of GO to reduced graphene oxide (rGO) [87]. The broad hump is a distinctive feature that reflects the amorphous nature of rGO. This occurs as a consequence of removing oxygen-containing functional groups from the graphene oxide layers during the reduction process**.** The diffraction peaks at $2\theta = 14.78°$, 28.82°, 32.01° and 33.35° are corresponding to the crystal planes of (002), (004), (100), (101) of crystalline WS_2 **[**82]. The diffraction peaks show that the composite material comprises well-ordered WS_2 with a hexagonal lattice structure. Thus, the XRD analysis confirms the presence of well-ordered crystal structures of AuNPs, rGO, and WS_2 in the ternary composite material. The distinctive peaks observed at $2\theta = 38.54°$ and 44.76° correspond to AuNPs and the broad hump near 24.17° corresponds to rGO. Additionally, the diffraction peaks at $2\theta = 14.78°$, 28.82°, 32.01°, and 33.35° indicate the

presence of crystalline WS_2 [88]. The XRD peaks offer crucial insights into the crystal structure and orientation of the composite material, which are of vital significance for future applications in photocatalysis, electronics, and energy storage.

5.5 Raman analysis

Raman spectroscopy is a highly useful method for investigating the structural characteristics of nanomaterials. This study used pure WS_2, a binary composite of WS_2/GO prepared by laser ablation, and a ternary composite of WS_2/GO/Au produced via a combination of laser ablation and hydrothermal methods.

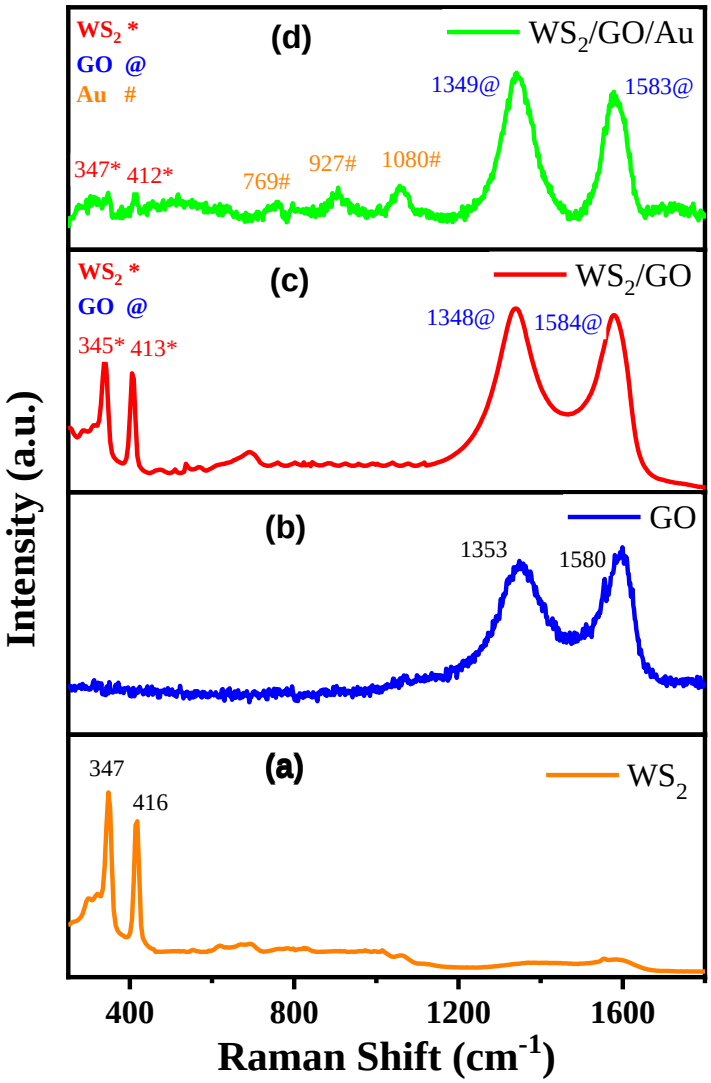

Fig. 21. (a) Raman spectra of GO, (b) WS_2, (c) WS_2/GO, (d) WS_2/GO/Au composite.

Fig. 21 (b) displays the raman spectrum of GO which often has two distinct peaks denoted by the D and G bands. The peak observed at ~ 1353 cm^{-1} belongs to the D band, which is attributed to the presence of defects and disorders in the graphene lattice. This peak, with a small intensity, is connected to the presence of sp^3 hybridized carbon atoms. On the other hand, the peak at about 1580 cm^{-1} is referred to as the G band, and it represents most noticeable feature in the raman spectrum of graphene-related materials. The G band corresponds to the in-plane vibrational motion of sp^2 hybridized carbon atoms in the graphene lattice. It is an indicator of the graphitic structure and shows that well-ordered carbon atoms are present. The bulk WS_2 sample exhibits two characteristic raman peaks at 347 cm^{-1} and 416 cm^{-1}, as seen in Fig. 21 (a). The peak identified at 347 cm^{-1} corresponds to the E_{2g} mode, which is the distinctive feature of the WS_2 crystalline structure. The peak shown at a wavenumber of 416 cm^{-1} is ascribed to the A_{1g} mode, which is also indicative of WS_2. These observed peaks match with the raman spectra reported in previous studies for bulk WS_2 [89-91]. The binary composite of WS_2/GO reveals four different Raman peaks at 345 cm^{-1}, 413 cm^{-1}, 1348 cm^{-1}, and 1584 cm^{-1}, as seen in Fig. 21 (c). [92]. The peaks at 345 cm^{-1} and 413 cm^{-1} belong to the E_{2g} and A_{1g} modes of WS_2, respectively. These peaks are similar to the ones seen in the pristine WS_2 sample. The peaks at 1348 cm^{-1} and 1584 cm^{-1} are ascribed to the D and G bands of GO, respectively. The D band represents the disorder-induced mode, while the G band corresponds to the sp^2 hybridization of carbon atoms in GO. In this study, the binary composite of WS_2/GO exhibited an ID/IG ratio of 1.03, confirming the presence of a certain amount of disorder or defects in the graphene oxide sheets. This outcome is anticipated due to the well-known presence of considerable amounts of oxygen-containing functional groups in GO, which have the potential to cause defects in the structure of graphene. Fig. 21 (d) illustrates the raman spectra of the ternary composite of WS_2/GO/Au, which reveals seven distinct peaks at 347 cm^{-1} 412 cm^{-1} 769 cm^{-1} 927 cm^{-1} 1080 cm^{-1} 1349 cm^{-1} and 1583 cm^{-1}. The smaller peaks at 347 cm^{-1} and 412 cm^{-1} are

the E_{2g} and A_{1g} modes of WS_2, and they are the same as those observed in the pure WS_2 sample. The small peaks at 769 cm^{-1} 927 cm^{-1} and 1080 cm^{-1} are caused by the Au-S stretching mode confirming the presence of Au nanoparticles in the composite material [93]. The peaks at 1349 cm^{-1} and 1583 cm^{-1} are ascribed to the D and G bands of GO, respectively, and are the same as those seen in the binary composite. The ternary composite of WS_2/GO/Au, exhibited a higher ID/IG ratio of 1.12, denoting an even higher degree of disorder or defects in the carbon-based components of the composite. An explanation for this phenomenon might be the incorporation Au nanoparticles into the composite, resulting in the disruption of the graphene structure and the creation of defects. Moreover, the hydrothermal synthesis technique used for fabricating the ternary composite could trigger the formation of defects due to the utilization of high temperature and pressure, which might potentially lead to alterations in the structure of the graphene oxide sheets. The increment in the ID/IG ratio from the binary to ternary composite indicates that the inclusion of Au nanoparticles and the hydrothermal synthesis technique have caused a rise in the degree of disorder or defects in the carbon-based components of the composite. This rise in disorder might be attributed to the presence of Au nanoparticles in the composite material, perhaps causing defects or disorder in the GO structure. In summary, the raman spectroscopic findings support the presence of WS_2, GO, and Au nanoparticles in the composite materials and provide valuable information on the structural characteristics of these materials. The ID/IG ratios observed in the GO in the binary and ternary composites indicate that the GO structure can be influenced by the other materials in the composite, and further studies and investigation are required to understand the scope of these effects fully.

5.6 Photocatalysis of nanocomposites with MB degradation

Because of their detrimental effects on ecosystems and human health, efficient photocatalysts are necessary to remove environmental pollutants. Therefore, in order to evaluate the photocatalytic properties of pristine WS_2, binary WS_2/GO composite, and ternary WS_2/GO/Au

composite for the degradation of MB under UV-light irradiation, we employed 300 mW LED light with a UV cut filter and checked the degradation at intervals of 10 minutes.

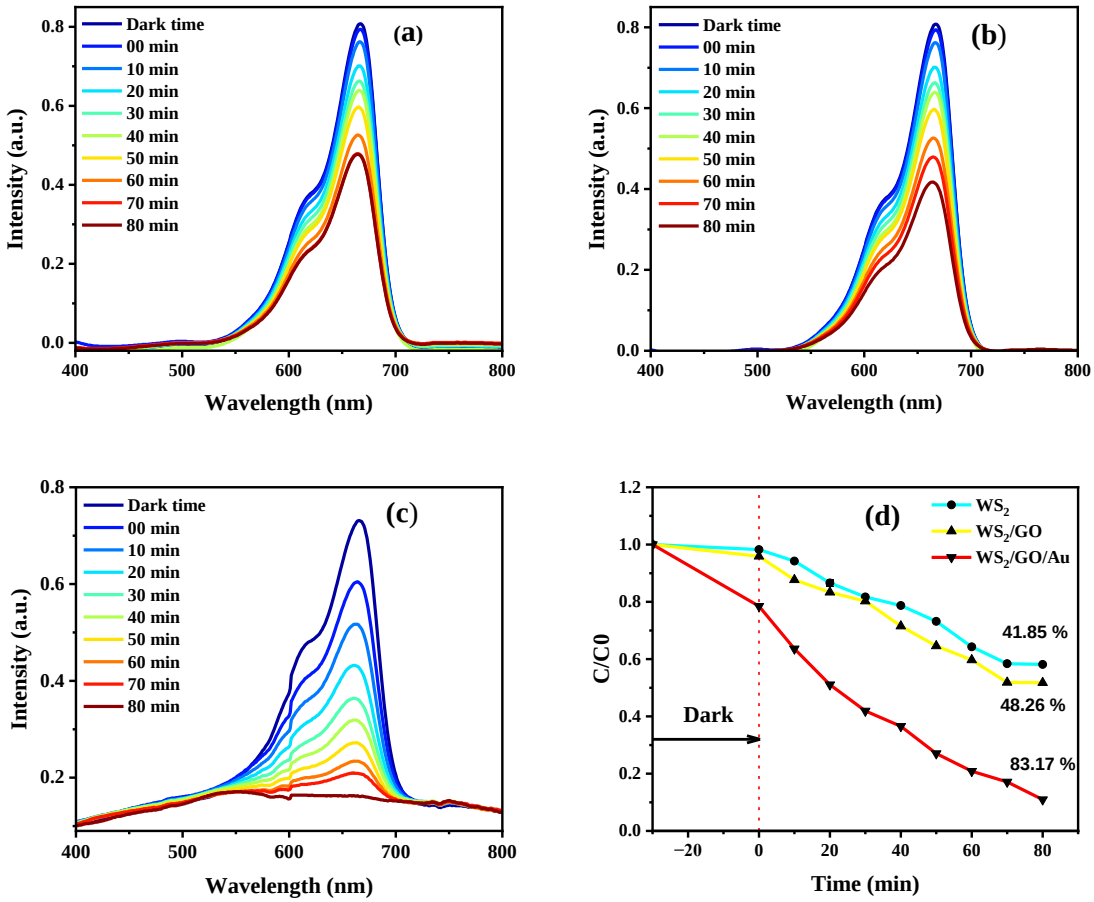

Fig. 22. Photocatalytic reduction of methylene blue using (a) WS_2 as catalyst, (b) WS_2/GO as catalyst, and (c) WS_2/GO/Au composite as catalyst and d) photocatalytic degradation efficiency of photocatalytic system.

According to Fig. 22 (a), the pristine WS_2 achieved a degradation efficiency of 41.85 % after being exposed to UV-light for a period of 80 minutes. As seen in Fig. 22 (b), the binary composite of WS_2/GO showed an enhanced efficiency of 48.27 %. On the other hand, as compared to the pristine WS_2 and binary WS_2/GO composite, the ternary composite of WS_2/GO/Au demonstrated a better efficiency of 83.17 % under the same experimental conditions as displayed in Fig. 22 (c). Finally, the ternary composite of WS_2/GO/Au demonstrated high photocatalytic activity for methylene blue degradation under UV-light irradiation, as illustrated in Fig. 22 (d) with photocatalytic degradation efficiency. The

increased absorbance range and higher electron-hole separation efficiency may be attributed to the synergistic actions of WS_2, GO, and Au. These findings indicate that the WS_2/GO/Au compound has significant promise as an efficient photocatalyst for applications in environmental remediation.

Degradation mechanism

The process of decomposition of WS_2/GO/Au under visible light is studied using N,N-dimethylformamide (N-DMF), water, and N-methyl-2-pyrrolidone (NMP) solutions, which are employed to create the ternary composite. The degradation mechanism of WS_2/GO/Au under visible light is an evolving procedure that includes many steps, as seen in Fig. 23. Nevertheless, the employment of N-DMF, water, and NMP solutions may optimize the efficiency by creating a more favorable environment for the formation of electron-hole pairs, the creation of oxygen reactive species, and the decomposition of biological contaminants.

Steps of the degradation mechanism:

1. **Photoexcitation of the photocatalyst:** When exposed to visible light, the WS_2/GO/Au composite absorbs photons and emits electron-hole (e^--h^+) pairs. The electrons undergo excitation from the valence band to the conduction band, while the holes remain in the valence band.
2. **Interfacial charge transfer:** The energized electrons in the conduction band have the ability to go to other components of the ternary composite photocatalyst, such as metal nanoparticles or semiconductor quantum dots. To put it simply, this is called charge transfer across interfaces. [94-95].
3. **Formation of reactive oxygen species:** Electrons and holes in the conduction and valence bands have the potential to interact with water molecules, resulting in the generation of reactive oxygen species (ROS), such as hydroxyl radicals (•OH) and superoxide anion radicals (O2•−). The highly reactive oxygen species (ROS) have the

ability to oxidize contaminants that are present on the surface of the ternary composite catalyst [96-97].

4. **Degradation of the pollutant:** The ROS may breakdown the adsorbed contaminant into harmless products by reacting with it. [98].

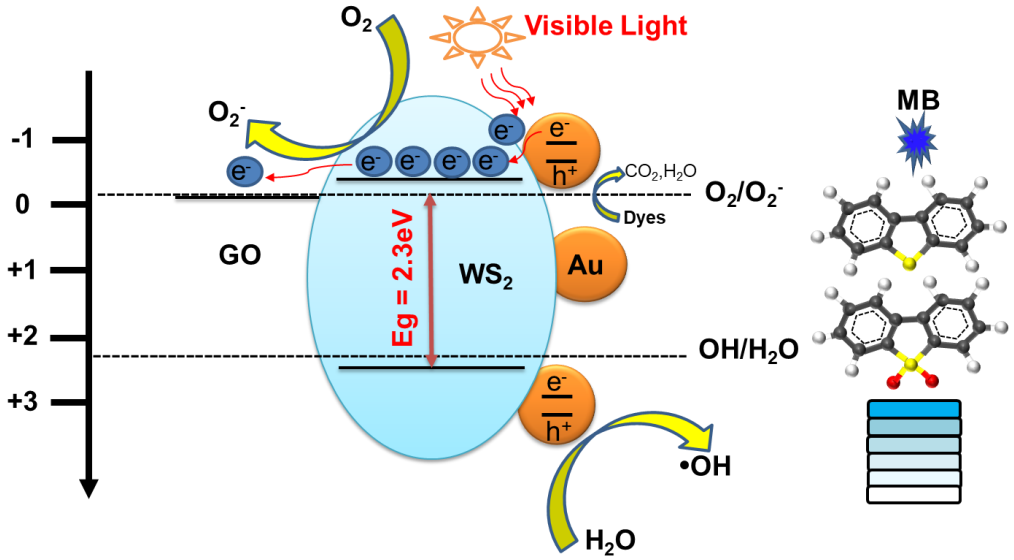

Fig. 23. Graphical illustration of photocatalysis of methylene blue by WS_2/GO/Au composite.

Chapter 6: Conclusion

This study used the laser ablation technique to produce WO_{3-x} petal-like nanosheets. The presence of a structure like a hump close to the 280 nm wavelength is indicative of the formation of WO_{3-x}. The XRD and EDS spectra showed that the bulk WS_2 was transformed into WO_{3-x}, or sub-oxide tungsten oxide. A self-assembling petal-like flake structure, potentially derived from ultra-thin WS2 nanosheets, is seen in the SEM images. As a result, a well-defined WO_{3-x} petal-like nanosheet might be utilized in potential optoelectronic device applications.

In continued research, we successfully synthesized the WO_{3-x}/SnO_2 composite using ns laser ablation in the liquid phase, and its photocatalytic performance has been studied by MB degradation. The UV-vis spectra of all the materials reveal their suitability for photocatalytic activity, which was subsequently evaluated by photocatalytic degradation of MB. EDS spectra illustrate the creation of WO_{3-x} from bulk WS_2 and nanocrystal octahedron structure SnO_2 from bulk SnO after ns laser ablation. Additionally, it also confirms the formation of compound WO_{3-x}/SnO_2 using elemental mapping. SEM images demonstrate a uniform distribution of nanometal-like structures in $WO_{3-x,}$ whereas as-synthesized SnO_2 exhibits octahedron crystal structure. The mixed morphology of these two materials has been found in binary composite WO_{3-x}/SnO_2. The peak intensity is enhanced in the XRD spectrum as a result of increased crystallinity. The photocatalytic activity was evaluated and compared by studying the photodegradation of MB using WO_{3-x}, SnO_2, and the binary composite. The WO_{3-x}/SnO_2 composite has the highest degradation efficiency of 84.4 %.

Further, additional research investigation suggests the production of a WS_2/GO/Au ternary composite by integrating WS_2 and GO via ns laser ablation, followed by the introduction of Au using the hydrothermal technique. The research finding demonstrates that the composite

material exhibits full optical absorption within the visible spectrum, making it a promising candidate for the degradation of pollutants. The composite was analyzed using spectroscopic and microscopic techniques, revealing the presence of a ternary composite consisting of WS_2/GO/Au. The WS_2 nanosheets were found to be well-mixed with Au nanoparticles on GO sheets. The composites that were developed showed enhanced photocatalytic activity for the breakdown of MB when exposed to UV light. This improvement may be ascribed to the unique shape and excellent ability to transport electrons of the composites. Hence, the WS_2/GO/Au composite has promising characteristics as a photoelectric material, making it suitable for experimental investigation in the field of photocatalysis.

References

1. Mei, X., Hu, T., Wang, Y., Weng, X., Liang, R., & Wei, M. (**2019**). Recent advancements in two dimensional nanomaterials for drug delivery. WIREs Nanomedicine and Nanobiotechnology, 12(2).
2. Bolotsky, A., Butler, D., Dong, C., Gerace, K., Glavin, N. R., Muratore, C., Robinson, J. A., & Ebrahimi, A. (**2019**). Two-Dimensional Materials in Biosensing and Healthcare: From In VitroDiagnostics to Optogenetics and Beyond. ACS Nano, 13(9), 9781–9810.
3. Carrow, J. K., Singh, K. A., Jaiswal, M. K., Ramirez, A., Lokhande, G., Yeh, A. T., Sarkar, T. R., Singh, I., & Gaharwar, A. K. (**2020**). Photothermal modulation of human stem cells using light-responsive 2D nanomaterials. Proceedings of the National Academy of Sciences, 117(24), 13329–13338.
4. Tao, W., Kong, N., Ji, X., Zhang, Y., Sharma, A., Ouyang, J., Qi, B., Wang, J., Xie, N., Kang, C., Zhang, H., Farokhzad, O. C., & Kim, J. S. (**2019**). Emerging two-dimensional monoelemental materials (Xenes) for biomedical applications. Chemical Society Reviews, 48(11), 2891–2912.
5. Baig, N. (**2023**). Two-dimensional nanomaterials: A critical review of recent progress, properties, applications, and future directions. Composites Part A: Applied Science and Manufacturing, 165, 107362.
6. Thiehmed, Z., Shakoor, A., & Altahtamouni, T. (**2021**). Recent Advances in WS_2 and Its Based Heterostructures for Water-Splitting Applications. Catalysts, 11(11), 1283.
7. Lai, Z., He, Q., Tran, T. H., Repaka, D. V. M., Zhou, D. D., Sun, Y., Xi, S., Li, Y., Chaturvedi, A., Tan, C., Chen, B., Nam, G. H., Li, B., Ling, C., Zhai, W., Shi, Z., Hu, D., Sharma, V., Hu, Z., .Zhang, H. (**2021**). Metastable 1T′-phase group VIB transition metal dichalcogenide crystals. Nature Materials, 20(8), 1113–1120.
8. Zhang, E., Xie, Y. M., Fang, Y., Zhang, J., Xu, X., Zou, Y. C., Leng, P., Gao, X. J., Zhang, Y., Ai, L., Zhang, Y., Jia, Z., Liu, S., Yan, J., Zhao, W., Haigh, S. J., Kou, X., Yang, J., Huang, F., Dong, S. (**2022**). Spin–orbit–parity coupled superconductivity in atomically thin 2M-WS_2. Nature Physics, 19(1), 106–113.
9. Han, B., & Hu, Y. H. (**2016**). MoS_2 as a co-catalyst for photocatalytic hydrogen production from water. Energy Science & Engineering, 4(5), 285–304.

10. Thomas, N., Mathew, S., Nair, K., O'Dowd, K., Forouzandeh, P., Goswami, A., McGranaghan, G., & Pillai, S. (**2021**). 2D MoS_2: structure, mechanisms, and photocatalytic applications. Materials Today Sustainability, 13, 100073.
11. Mak, K. F., Lee, C., Hone, J., Shan, J., & Heinz, T. F. (**2010**). Atomically ThinMoS_2: A New Direct-Gap Semiconductor. Physical Review Letters, 105(13).
12. Splendiani, A., Sun, L., Zhang, Y., Li, T., Kim, J., Chim, C. Y., Galli, G., & Wang, F. (**2010**). Emerging Photoluminescence in Monolayer MoS_2. Nano Letters, 10(4), 1271–1275.
13. Cong, C., Shang, J., Wang, Y., & Yu, T. (**2017**). Optical Properties of 2D Semiconductor WS_2. Advanced Optical Materials, 6(1).
14. Sachin, S., Kumari, P., Gupta, N., Rani, S., Kar, S., & Ray, S. J. (**2023**). Van der Waals twistronics in a MoS_2/WS_2 heterostructure. Computational Condensed Matter, 35, e00797.
15. Zhao, D., Sheng, G., Chen, C., & Wang, X. (**2012**). Enhanced photocatalytic degradation of methylene blue under visible irradiation on graphene@TiO_2 dyade structure. Applied Catalysis B: Environmental, 111–112, 303–308.
16. Wang, L., Wang, Y., Xu, T., Liao, H., Yao, C., Liu, Y., Li, Z., Chen, Z., Pan, D., Sun, L., & Wu, M. (**2014**). Gram-scale synthesis of single-crystalline graphene quantum dots with superior optical properties. Nature Communications, 5(1).
17. Wang, H., Robinson, J. T., Diankov, G., & Dai, H. (**2010**). Nanocrystal Growth on Graphene with Various Degrees of Oxidation. Journal of the American Chemical Society, 132(10), 3270–3271.
18. Li, X., Wang, Q., Zhao, Y., Wu, W., Chen, J., & Meng, H. (**2013**). Green synthesis and photo-catalytic performances for ZnO-reduced graphene oxide nanocomposites. Journal of Colloid and Interface Science, 411, 69–75.
19. Raidongia, K., Tan, A. T., & Huang, J. (**2014**). Graphene Oxide: Some New Insights into an Old Material. Carbon Nanotubes and Graphene, 341–374.
20. Ayub, M., & Othman, M. H. D. (**2023**). Graphene oxide-based nano filtration membranes for separation of heavy metals. Emerging Techniques for Treatment of Toxic Metals From Wastewater, 231–288.
21. Li, S., Huang, L., Wang, D., Zhou, S., Sun, X., Zhao, R., Wang, G., Yao, T., Zhao, K., & Chen, R. (**2023**). A review of 3D superhydrophilic porous materials for oil/water separation. Separation and Purification Technology, 326, 124847.

22. Robinson, J. T., Perkins, F. K., Snow, E. S., Wei, Z., & Sheehan, P. E. (**2008**). Reduced Graphene Oxide Molecular Sensors. Nano Letters, 8(10), 3137–3140.
23. Pandey, A., & Chauhan, P. (**2023**). Functionalized graphene nanomaterials: Next-generation nanomedicine. Functionalized Carbon Nanomaterials for Theranostic Applications, 3–18.
24. Furube, A., Du, L., Hara, K., Katoh, R., & Tachiya, M. (**2007**). Ultrafast Plasmon-Induced Electron Transfer from Gold Nanodots into TiO_2 Nanoparticles. Journal of the American Chemical Society, 129(48), 14852–14853.
25. Sylvestre, J. P., Poulin, S., Kabashin, A. V., Sacher, E., Meunier, M., & Luong, J. H. T. (**2004**). Surface Chemistry of Gold Nanoparticles Produced by Laser Ablation in Aqueous Media. The Journal of Physical Chemistry B, 108(43), 16864–16869.
26. Hu, J., Karam, T. E., Blake, G. A., & Zewail, A. H. (**2017**). Ultrafast lattice dynamics of single crystal and polycrystalline gold nanofilms. Chemical Physics Letters, 683, 258–261.
27. Larm, N. E., Essner, J. B., Pokpas, K., Canon, J. A., Jahed, N., Iwuoha, E. I., & Baker, G. A. (**2018**). Room-Temperature Turkevich Method: Formation of Gold Nanoparticles at the Speed of Mixing Using Cyclic Oxocarbon Reducing Agents. The Journal of Physical Chemistry C, 122(9), 5105–5118.
28. Nasiri, P., Doranian, D., & Sari, A. H. (**2019**). Synthesis of Au/Si nanocomposite using laser ablation method. Optics & Laser Technology, 113, 217–224.
29. Baigent, C. L., & Müller, G. (1980, April). A colloidal gold prepared with ultrasonics. Experientia, 36(4), 472–473.
30. Martin, M. N., Basham, J. I., Chando, P., & Eah, S. K. (**2010**). Charged Gold Nanoparticles in Non-Polar Solvents: 10-min Synthesis and 2D Self-Assembly. Langmuir, 26(10), 7410–7417.
31. Niu, Z., & Li, Y. (**2013**). Removal and Utilization of Capping Agents in Nanocatalysis. Chemistry of Materials, 26(1), 72–83.
32. Brust, M., Walker, M., Bethell, D., Schiffrin, D. J., & Whyman, R. (**1994**). Synthesis of thiol-derivatised gold nanoparticles in a two-phase Liquid–Liquid system. J. Chem. Soc., Chem. Commun., 0(7), 801–802.
33. Turkevich, J., Stevenson, P. C., & Hillier, J. (**1951**). A study of the nucleation and growth processes in the synthesis of colloidal gold. Discussions of the Faraday Society, 11, 55.

34. Das, S., Kim, M., Lee, J. W., & Choi, W. (**2014**). Synthesis, Properties, and Applications of 2-D Materials: A Comprehensive Review. Critical Reviews in Solid State and Materials Sciences, 39(4), 231–252.
35. Niemax, K. (**2001**). Laser ablation - reflections on a very complex technique for solid sampling. Fresenius' Journal of Analytical Chemistry, 370(4), 332–340.
36. Pacella, C. M., Breschi, L., Bottacci, D., & Masotti, L. (**2019**). Physical Principles of Laser Ablation. Image-Guided Laser Ablation, 7–18.
37. Rezk, R. A., Abdel Ghany, N. A., & Mostafa, A. M. (**2022**). Laser-Assisted Method for Cleaning and Analysis of Archaeological Metallic Coins. Coatings, 12(10), 1548.
38. Zhengjia, L., Xinju, L., & Zhaide, W. (**1986**). Application of Nd:YAG Laser in Medical Science Area, Waidelich, W., Kiefhaber, P. (eds), Laser/Optoelectronics in Medicine/Laser/Optoelektronik in Der Medizin, Springer, Berlin, Heidelberg ,267–267
39. Morsi, M., Asnag, G., Rajeh, A., & Awwad, N. S. (**2021**). Nd:YAG nanosecond laser induced growth of Au nanoparticles within CMC/PVA matrix: Multifunctional nanocomposites with tunable optical and electrical properties. Composites Communications, 24, 100662.
40. Afifi, H. A. M., Abdel-Ghani, M., Mahmoud, R., Alkallas, F. H., Trabelsi, A. B. G., & Mostafa, A. M. (**2023**). Comparative Study between First and Second Harmonics of a Nd:YAG Laser for Cleaning Manifestation Damages That Appeared in Pigments Used on Archaeological Cartonnage. Micromachines, 14(7), 1415.
41. Liu, H. Y., Zhou, Z. H., Bian, Q., Bo, Y., Kou, Y., Yuan, L., Cui, D. F., & Peng, Q. J. (**2023**). High-Efficiency Nanosecond Green Laser Based on Extra-Cavity Second-Harmonic Generation of a Nd:YAG MOPA System. IEEE Photonics Journal, 15(5), 1–5.
42. Romanos, G. (**1994**). Clinical Applications of the Nd:YAG Laser in Oral Soft Tissue Surgery and Periodontology. Journal of Clinical Laser Medicine & Surgery, 12(2), 103–108.
43. Chaluvadi, S. K., Punathum Chalil, S., Mazzola, F., Dolabella, S., Rajak, P., Ferrara, M., Ciancio, R., Fujii, J., Panaccione, G., Rossi, G., & Orgiani, P. (**2023**). Nd:YAG infrared laser as a viable alternative to excimer laser: YBCO case study. Scientific Reports, 13(1).
44. Chaluvadi, S. K., Mondal, D., Bigi, C., Knez, D., Rajak, P., Ciancio, R., Fujii, J., Panaccione, G., Vobornik, I., Rossi, G., & Orgiani, P. (**2021**). Pulsed laser deposition

of oxide and metallic thin films by means of Nd:YAG laser source operating at its 1st harmonics: recent approaches and advances. Journal of Physics: Materials, 4(3), 032001.

45. Petronic, S., Stevic, Z., Dimitrijevic, S., Rajcic, B., & Milovanovic, D. (**2020**). Application of semiconductor continuous and Nd:YAG pulsed laser processing for nondestructive cleaning of the historical paper. Journal of Laser Applications, 32, 032024.
46. Medvid, A., Mycko, A., Onufrijevs, P., & Daukst, E. (**2012**). Application of Nd:YAG Laser in Semiconductors' Nanotechnology. Nd YAG Laser.
47. Rashid, S. N., & Jasim, A. S. (**2023**). Effect of Nd:YAG laser on the optical properties of nanoparticle CuO solutions. Materials Today: Proceedings, 80, 3909–3912.
48. Yang, G., & Park, S. J. (**2019**). Conventional and Microwave Hydrothermal Synthesis and Application of Functional Materials: A Review. Materials, 12(7), 1177.
49. Jones, A. C., & Chalker, P. R. (**2003**). Some recent developments in the chemical vapour deposition of electroceramic oxides. Journal of Physics D: Applied Physics, 36(6), R53–R79.
50. Wang, W. N., Lenggoro, I. W., Terashi, Y., Kim, T. O., & Okuyama, K. (**2005**). One-step synthesis of titanium oxide nanoparticles by spray pyrolysis of organic precursors. Materials Science and Engineering: B, 123(3), 194–202.
51. Li, H., Cheng, B., Zhang, J., Zhou, X., Shi, C., Zeng, L., & Wang, C. (**2023**). Recent advances in the application of bismuth-based catalysts for degrading environmental emerging organic contaminants through photocatalysis: A review. Journal of Environmental Chemical Engineering, 11(5), 110371.
52. Pattnaik, A., Sahu, J., Poonia, A. K., & Ghosh, P. (**2023**). Current perspective of nano-engineered metal oxide based photocatalysts in advanced oxidation processes for degradation of organic pollutants in wastewater. Chemical Engineering Research and Design, 190, 667–686.
53. Van Thuan, D., Ngo, H. L., Thi, H. P., & Chu, T. T. H. (**2023**). Photodegradation of hazardous organic pollutants using titanium oxides -based photocatalytic: A review. Environmental Research, 229, 116000.
54. Zhang, J., Li, L., Du, M., Cui, Y., Li, Y., Yan, W., Huang, H., Li, X., & Zhu, X. (**2023**). Single-Atom Phosphorus Defects Decorated CoP Cocatalyst Boosts Photocatalytic Hydrogen Generation Performance of Cd0.5Zn0.5S by Directed Separating the Photogenerated Carriers. Small, 19(20).

55. Navakoteswara Rao, V., Lakshmana Reddy, N., Preethi, V., Karthik, M., Yu, Y. T., Yang, J. M., Mamatha Kumari, M., & Shankar, M. (**2023**). A critical review on core/shell-based nanostructured photocatalysts for improved hydrogen generation. International Journal of Hydrogen Energy, 48(31), 11754–11774.
56. Üstünel, T., Ide, Y., Kaya, S., & Doustkhah, E. (**2023**). Single-Atom Sn-Loaded Exfoliated Layered Titanate Revealing Enhanced Photocatalytic Activity in Hydrogen Generation. ACS Sustainable Chemistry & Engineering, 11(8), 3306–3315.
57. Sinopoli, A., Othman, Z., Rasool, K., & Mahmoud, K. A. (**2019**). Electrocatalytic/photocatalytic properties and aqueous media applications of 2D transition metal carbides (MXenes). Current Opinion in Solid State and Materials Science, 23(5), 100760.
58. Yemmireddy, V. K., & Hung, Y. C. (**2017**). Using Photocatalyst Metal Oxides as Antimicrobial Surface Coatings to Ensure Food Safety-Opportunities and Challenges. Comprehensive Reviews in Food Science and Food Safety, 16(4), 617–631.
59. Xiong, J., Di, J., Xia, J., Zhu, W., & Li, H. (**2018**). Surface Defect Engineering in 2D Nanomaterials for Photocatalysis. Advanced Functional Materials, 28(39).
60. Huang, H., Lei, Y., Bai, L., Liang, Y., & Yang, H. (**2023**). Morphology-dependent quasi 2D/2D point-flat-plate ternary CdS/MoS_2/WS_2 heterojunction with improved visible photocatalytic degradation of tetracycline. Colloids and Surfaces A: Physicochemical and Engineering Aspects, 657, 130558.
61. Aswal, D., Bamola, P., Rani, C., Rawat, S., Bhatt, A., Chhoker, S., Sharma, M., Dwivedi, C., Kumar, R., & Sharma, H. (**2023**). Enhanced Photocatalytic Activity in 2D-1D WS_2/TiO_2 and 2D-2D MoS_2/WS_2 Heterosystems. ChemistrySelect, 8(34).
62. Famili, Z., Dorranian, D., & Sari, A. H. (**2020**). Laser ablation-assisted synthesis of tungsten sub-oxide (W17O47) nanoparticles in water: effect of laser fluence. Optical and Quantum Electronics, 52(6).
63. Afify, H., Hassan, S., Obaida, M., Moussa, I., & Abouelsayed, A. (**2019**). Preparation, characterization, and optical spectroscopic studies of nanocrystalline tungsten oxide WO_3. Optics & Laser Technology, 111, 604–611.
64. Lv, Y., Duan, S., & Wang, R. (**2020**). Structure design, controllable synthesis, and application of metal-semiconductor heterostructure nanoparticles. Progress in Natural Science: Materials International, 30(1), 1–12.
65. Huirache-Acuña, R., Paraguay-Delgado, F., Albiter, M. A., Alvarez-Contreras, L., Rivera-Muñoz, E. M., & Alonso-Núñez, G. (**2009**). Synthesis and characterization of

WO_3 and WS_2 hexagonal phase nanostructures and catalytic test in sulfur remotion. Journal of Materials Science, 44(16), 4360–4369.

66. Hu, X., Song, G., Li, W., Peng, Y., Jiang, L., Xue, Y., Liu, Q., Chen, Z., & Hu, J. (**2013**). Phase-controlled synthesis and photocatalytic properties of SnS, SnS_2 and SnS/SnS_2 heterostructure nanocrystals. Materials Research Bulletin, 48(6), 2325–2332.
67. Famili, Z., Dorranian, D., & Sari, A. H. (**2020**). Laser ablation-assisted synthesis of tungsten sub-oxide ($W_{17}O_{47}$) nanoparticles in water: effect of laser fluence. Optical and Quantum Electronics, 52.
68. Adeyemi, J. O., & Onwudiwe, D. C. (**2020**). SnS_2 and SnO_2 Nanoparticles Obtained from Organotin(IV) Dithiocarbamate Complex and Their Photocatalytic Activities on Methylene Blue. Materials, 13(12), 2766.
69. Gupta, P., Lapalikar, V., Kundu, R., & Balasubramanian, K. (**2016**). Recent Advances in Membrane Based Waste Water Treatment Technology: A Review. Energy and Environment Focus, 5(4), 241–267.
70. Huang, X., & Nan, Z. (**2020**). Formation of octahedron-shaped $ZnFe_2O_4/SiO_2$ with yolk–shell structure. Journal of Physics and Chemistry of Solids, 141, 109410.
71. Xue, X. Y., He, B., Yuan, S., Xing, L. L., Chen, Z. H., & Ma, C. H. (**2011**). SnO_2/WO_3 core–shell nanorods and their high reversible capacity as lithium-ion battery anodes. Nanotechnology, 22(39), 395702.
72. Garde A.S., (**2015**).Electrical and Structural Properties of WO_3-SnO_2 Thick-Film resistors Prepared by Screen Printing Technique, Research Journal of Recent Sciences, 4, 55-61.
73. Zhang, Y. C., Du, Z. N., Li, S. Y., & Zhang, M. (**2010**). Novel synthesis and high visible light photocatalytic activity of SnS2 nanoflakes from $SnCl_2{\cdot}2H_2O$ and S powders. Applied Catalysis B: Environmental, 95(1–2), 153–159.
74. Muhd Julkapli, N., Bagheri, S., & Bee Abd Hamid, S. (**2014**). Recent Advances in Heterogeneous Photocatalytic Decolorization of Synthetic Dyes. The Scientific World Journal, 25054183, 1–25.
75. Lam, S. M., Sin, J. C., Abdullah, A. Z., & Mohamed, A. R. (**2012**). Degradation of wastewaters containing organic dyes photocatalysed by zinc oxide: a review. Desalination and Water Treatment, 41(1–3), 131–169.
76. Xie, Y., Zhang, C., Miao, S., Liu, Z., Ding, K., Miao, Z., An, G., & Yang, Z. (**2008**). One-pot synthesis of ZnS/polymer composites in supercritical CO_2–ethanol solution

and their applications in degradation of dyes. Journal of Colloid and Interface Science, 318(1), 110–115.

77. Sharma, M., Jain, T., Singh, S., & Pandey, O. (**2012**). Photocatalytic degradation of organic dyes under UV–Visible light using capped ZnS nanoparticles. Solar Energy, 86(1), 626–633.
78. Pradhan, G., & Sharma, A. K. (**2019**). Linear and nonlinear optical response of sulfur-deficient nanocrystallite WS_2 thin films. Journal of Materials Science, 54(24), 14809–14824.
79. Gurunathan, S., Woong Han, J., Abdal Daye, A., Eppakayala, V., & Kim, J. H. (**2012**). Oxidative stress-mediated antibacterial activity of graphene oxide and reduced graphene oxide in Pseudomonas aeruginosa. International Journal of Nanomedicine, 5901.
80. Feng, D. N., Fang, A. S., Zhang, T. Y., Ma, M. Z., Xu, Z. H., Sun, Y. X., Zhang, M. T., & Shi, F. (**2021**). Green synthesis and characterization of gold nanoparticles and their application for the rapid detection of glycyrrhizin with immunochromatographic strips. RSC Advances, 11(39), 23851–23859.
81. Huang, F., Jian, J., & Wu, R. (**2016**). Few-layer thick WS_2 nanosheets produced by intercalation/exfoliation route. Journal of Materials Science, 51(22), 10160–10165.
82. Qin, Y. Q., Peng, Y. Q., Yang, W. F., Wang, Y., Cui, J. W., & Zhang, Y. (**2020**). Ultrathin exfoliated WS_2 nanosheets in low-boiling-point solvents for high-efficiency hydrogen evolution reaction. IOP Conference Series: Materials Science and Engineering, 770, 012079.
83. Kumar, A., Sadanandhan, A. M., & Jain, S. L. (**2019**). Silver doped reduced graphene oxide as a promising plasmonic photocatalyst for oxidative coupling of benzylamines under visible light irradiation. New Journal of Chemistry, 43(23), 9116–9122.
84. Mulik, B. B., Bankar, B. D., Munde, A. V., Biradar, A. V., & Sathe, B. R. (**2020**). Bismuth-Oxide Decorated Graphene Oxide Hybrids for Catalytic and Electrocatalytic Reduction of CO_2. Chemistry − European Journal, 26(40), 8801−8809.
85. Li, Z., Lu, C., Xia, Z., Zhou, Y., & Luo, Z. (**2007**). X-ray diffraction patterns of graphite and turbostratic carbon. Carbon, 45(8), 1686–1695.
86. Krishnamurthy, S., Esterle, A., Sharma, N. C., & Sahi, S. V. (**2014**). Yucca-derived synthesis of gold nanomaterial and their catalytic potential. Nanoscale Research Letters, 9, 627.

87. Zheng, P., Liu, T., Su, Y., Zhang, L., & Guo, S. (**2016**). TiO_2 nanotubes wrapped with reduced graphene oxide as a high-performance anode material for lithium-ion batteries. Scientific Reports, 6, 36580.
88. Qin, Y. Q., Peng, Y. Q., Yang, W. F., Wang, Y., Cui, J. W., & Zhang, Y. (**2020**). Ultrathin exfoliated WS_2 nanosheets in low-boiling-point solvents for high-efficiency hydrogen evolution reaction. IOP Conference Series: Materials Science and Engineering, 770, 012079.
89. Hussain, S., Vikraman, D., Ali Sheikh, Z., Taqi Mehran, M., Shahzad, F., Mujasam Batoo, K., Kim, H. S., Kim, D. K., Ali, M., & Jung, J. (**2023**). WS_2-embedded MXene/GO hybrid nanosheets as electrodes for asymmetric supercapacitors and hydrogen evolution reactions. Chemical Engineering Journal, 452, 139523.
90. Sinha, S., Sathe, V., & Arora, S. K. (**2019**). Temperature dependent Raman investigations of few-layered WS_2 nanosheets. Solid State Communications, 298, 113626.
91. Berkdemir, A., Gutiérrez, H. R., Botello-Méndez, A. R., Perea-López, N., Elías, A. L., Chia, C. I., Wang, B., Crespi, V. H., López-Urías, F., Charlier, J. C., Terrones, H., & Terrones, M. (**2013**). Identification of individual and few layers of WS_2 using Raman Spectroscopy. Scientific Reports, 3, 1755.
92. Li, Y., Zhou, Y., Wang, Y., Liu, M., Yuan, J., & Men, X. (**2021**). Facile synthesis of WS_2@GO nanohybrids for significant improvement in mechanical and tribological performance of EP composites. Tribology International, 163, 107148.
93. He, X. N., Gao, Y., Mahjouri-Samani, M., Black, P. N., Allen, J., Mitchell, M., Xiong, W., Zhou, Y. S., Jiang, L., & Lu, Y. F. (**2012**). Surface-enhanced Raman spectroscopy using gold-coated horizontally aligned carbon nanotubes. Nanotechnology, 23(20), 205702.
94. Mohanta, D., & Ahmaruzzaman, M. (**2020**). A novel Au-SnO_2-rGO ternary nanoheterojunction catalyst for UV-LED induced photocatalytic degradation of clothianidin: Identification of reactive intermediates, degradation pathway and in-depth mechanistic insight. Journal of Hazardous Materials, 397, 122685.
95. Mohanta, D., & Ahmaruzzaman, M. (**2020**). Biogenic synthesis of SnO_2 quantum dots encapsulated carbon nanoflakes: An efficient integrated photocatalytic adsorbent for the removal of bisphenol A from aqueous solution. Journal of Alloys and Compounds, 828, 154093.

96. Cui, Y., Lin, C., Li, M., Zhu, N., Meng, J., & Zhao, J. (**2022**). $CuWO_4$/CuS heterojunction photocatalyst for the application of visible-light-driven photodegradation of dye pollutions. Journal of Alloys and Compounds, 893, 162181.
97. Hong, X., Wang, X., Li, Y., Fu, J., & Liang, B. (**2020**). Progress in Graphene/Metal Oxide Composite Photocatalysts for Degradation of Organic Pollutants. Catalysts, 10(8), 921.
98. Pavel, M., Anastasescu, C., State, R. N., Vasile, A., Papa, F., & Balint, I. (**2023**). Photocatalytic Degradation of Organic and Inorganic Pollutants to Harmless End Products: Assessment of Practical Application Potential for Water and Air Cleaning, Catalysts, 13(2), 380.

Research activity

Academic Research Paper:

1. Vinayak B. Shinde, Yasuyuki Maeda, Tetsuro Katayama, Akihiro Furube, Takaaki Yano, and Pankaj Koinkar, **"Tungsten suboxide (WO_{3-x}) petal-like nanosheets created by laser ablation method"**, *Modern Physics Letters B, Vol. 37, No. 16 (2023) 2340005 DOI: 10.1142/S0217984923400055*

2. Vinayak Shinde, Tetsuro Katayama, Yasuyuki Maeda, Satoshi Sugano, Akihiro Furube and Pankaj Koinkar, "**Approach for Achieving Effective Photocatalytic Activity Under Visible Light of WO_{3-x}/SnO_2 Produced by Laser Ablation Method",** *Springer Proceedings in Physics: Proceedings of the 3rd International Conference on Nanomaterials and Advanced Composites (NAC 2022) Vol. 298 (Nov. 2023) 75 -84 https://link.springer.com/book/9789819971527*

3. Vinayak B. Shinde, Pratiksha Tanwade, Tetsuro Katayama, Akihiro Furube, Bhaskar Sathe, and Pankaj Koinkar, "**A Ternary Composite WS_2/GO/Au Synthesized from Combination of Laser Ablation and Hydrothermal Method for Photo and Electrochemical Degradation of Methylene Blue"** Surfaces and Interfaces (under review).

Presentations at International Conference

1. Vinayak Shinde, Tetsuro Katayama, Yasuyuki Maeda, Satoshi Sugano, Akihiro Furube and Pankaj Koinkar, "**Photocatalytic performance under visible light of WO_{3-x}/ SnO_2 synthesized by laser ablation method**", *3rd International Conference on Nanomaterials and Advanced Composites (NAC 2022), Tokushima, Japan, July15-17, 2022:* ***Oral.***

2. Vinayak Shinde, Pankaj Koinkar, Tetsuro Katayama, and Akihiro Furube, **Comparative study of methylene blue (MB) degradation using WS_2, WS_2/GO, and WS_2/GO/Au composites prepared by laser ablation and hydrothermal methods**, *pLED International Symposium 2023: Exploring Invisible Light Technology", Tokushima, Japan, March 4-5, 2023.* ***Poster.***

3. Vinayak Shinde, Tetsuro Katayama, Akihiro Furube, Pankaj Koinkar, **"Plasmonic Au Nanoparticles Decorated MoS_2@GO for Efficient Photocatalytic Methylene Blue Degradation"**, *International conference on Nanomaterials and Nanotechnology (ICNN-2023), Nagpur, India, September 11-13,2023,* ***Poster****.*

Awards

1. **Best paper presentation Award**; Vinayak Shinde, Tetsuro Katayama, Yasuyuki Maeda, Satoshi Sugano, Akihiro Furube, and Pankaj Koinkar, "**Photocatalytic performance under visible light of WO_{3-x}/ SnO_2 synthesized by laser ablation method**" *NAC 2022 Proceedings of the 2nd International Conference on Nanomaterials and Advanced Composite. Tokushima, Japan, July15-17, 2022.*

2. **Best poster presentation Award**; Vinayak Shinde, Pankaj Koinkar, Tetsuro Katayama, and Akihiro Furube, **Comparative study of methylene blue (MB) degradation using WS_2, WS_2/GO, and WS_2/GO/Au composites prepared by laser ablation and hydrothermal methods**, *pLED International Symposium 2023: Exploring Invisible Light Technology", Tokushima, Japan, March 4-5, 2023.*

3. "**Heiwa-Nakajima Scholarship**" from *Heiwa-Nakajima Foundation, received from April 2023 to March 2024.*

Research Internship

1. **"Study of 5G networks, optical fiber networks and its installation",** CATV Ltd.**,** Matsuyama, Ehime, Japan, August 28- September 01, 2023.